

Energetic ion transport by microturbulence is insignificant in tokamaks^{a)}

D. C. Pace (庞大卫),^{1,b)} M. E. Austin,² E. M. Bass,³ R. V. Budny,⁴ W. W. Heidbrink,⁵ J. C. Hillesheim,⁶ C. T. Holcomb,⁷ M. Gorelenkova,⁴ B. A. Grierson,⁴ D. C. McCune,⁴ G. R. McKee,⁸ C. M. Muscatello,⁵ J. M. Park,⁹ C. C. Petty,¹ T. L. Rhodes,⁶ G. M. Staebler,¹ T. Suzuki,¹⁰ M. A. Van Zeeland,¹ R. E. Waltz,¹ G. Wang,⁶ A. E. White,¹¹ Z. Yan,⁸ X. Yuan,⁴ and Y. B. Zhu⁵

¹General Atomics, PO Box 85608, San Diego, California 92186-5608, USA

²University of Texas-Austin, 2100 San Jacinto Blvd, Austin, Texas 78712-1047, USA

³University of California, San Diego, 9500 Gilman Dr., La Jolla, California 92093-0417, USA

⁴Princeton Plasma Physics Laboratory, PO Box 451, Princeton, New Jersey 08543-0451, USA

⁵University of California, Irvine, University Dr., Irvine, California 92697, USA

⁶University of California, Los Angeles, PO Box 957099, Los Angeles, California 90095-7099, USA

⁷Lawrence Livermore National Laboratory, 7000 East Ave, Livermore, California 94550-9234, USA

⁸University of Wisconsin-Madison, 1500 Engineering Dr., Madison, Wisconsin 53706, USA

⁹Oak Ridge National Laboratory, PO Box 2008, Oak Ridge, Tennessee 37831, USA

¹⁰Japan Atomic Energy Agency, 801-1, Mukoyama, Naka, Ibaraki-ken 311-0193, Japan

¹¹Massachusetts Institute of Technology, 77 Massachusetts Ave, Cambridge, Massachusetts 02139, USA

(Received 14 December 2012; accepted 8 March 2013; published online 7 May 2013)

Energetic ion transport due to microturbulence is investigated in magnetohydrodynamic-quiescent plasmas by way of neutral beam injection in the DIII-D tokamak [J. L. Luxon, Nucl. Fusion **42**, 614 (2002)]. A range of on-axis and off-axis beam injection scenarios are employed to vary relevant parameters such as the character of the background microturbulence and the value of E_b/T_e , where E_b is the energetic ion energy and T_e the electron temperature. In all cases, it is found that any transport enhancement due to microturbulence is too small to observe experimentally. These transport effects are modeled using numerical and analytic expectations that calculate the energetic ion diffusivity due to microturbulence. It is determined that energetic ion transport due to coherent fluctuations (e.g., Alfvén eigenmodes) is a considerably larger effect and should therefore be considered more important for ITER. © 2013 AIP Publishing LLC.

<http://dx.doi.org/10.1063/1.4803930>

I. INTRODUCTION

The viability of the tokamak¹ approach to fusion energy is dependent on the ability to magnetically confine fusion-produced α -particles such that they transfer their energy to the background plasma and thereby sustain a burning regime. In addition to α -particles, present day tokamaks and ITER² are concerned with the transport properties of energetic ions sourced by auxiliary heating and current drive methods such as neutral beam injection (NBI) and ion cyclotron resonance heating (ICRH). For NBI and ICRH, energetic ion confinement determines the efficiency of current drive or heating. A great deal of attention is now given to the transport effects of coherent modes that are driven by the energetic ion population, such as Alfvén eigenmodes³ (AEs). Indeed, reviews of the status of energetic ion research have evolved from basic principles⁴ to a focus on Alfvénic physics.⁵

A recent joint experiment⁶ conducted through the International Tokamak Physics Activity (ITPA) directed attention to the possibility that microturbulence significantly enhances neutral beam ion diffusion in cases of off-axis neutral beam current drive (NBCD). Conceptually, this occurs because off-axis neutral beam injection places a large

population of beam ions in the mid-radius region of the plasma where microturbulence is strong. On-axis NBCD, by contrast, is centrally peaked, thereby placing beam ions in the region where microturbulence is weak or nonexistent. New results show that measured radial profiles of off-axis NBCD agree with modeled expectations over an ITER relevant parameter range in high performance plasmas.⁷ The results shown in the present paper are concerned with lower confinement (L-mode) plasmas in which large amplitude microturbulence is present. Off-axis and on-axis NBI is used, alongside detailed measurements of the beam ion and plasma profiles, to investigate the possible contribution of microturbulence to the transport of energetic ions. To experimentally isolate microturbulence-induced beam ion transport requires the absence of magnetohydrodynamic (MHD) activity, such as Alfvén eigenmodes and sawtooth oscillations. Such MHD-quiescent tokamak plasmas from DIII-D^{8,9} are presented in this work, and the resulting analysis of energetic ion transport indicates that microturbulence is an insignificant transport mechanism for the energetic ion population.

This paper is organized as follows: Sec. II gives a review of experimental and theoretical results concerning energetic ion transport and the possible effects of microturbulence. The experimental setup, including diagnostics and NBI geometry, is given in Sec. III. Results from off-axis

^{a)}Paper JI2 5, Bull. Am. Phys. Soc. **57**, 151 (2012).

^{b)}Invited speaker. Electronic mail: pacedc@fusion.gat.com

NBI are given in Sec. IV, followed by on-axis NBI results in Sec. V. The discussion of Sec. VI summarizes the results, treats previously reported experimental results, and considers the difficulties in investigating the “low-energy” region of the energetic ion population. Finally, the conclusions are presented in Sec. VII.

II. BACKGROUND

Given that previous reviews^{4,5} of energetic ion transport in tokamaks have neglected the effects of microturbulence, we present here a review of experimental and theoretical results in this context. The intention is to demonstrate both the strong theoretical basis for interaction between energetic ions and small-scale fluctuations, and the large body of experimental work that indicates these interactions lead to insignificant changes in tokamak plasma behavior. It remains to be seen whether microturbulence effects on energetic ions will be fundamentally different in the burning plasma regime achieved in ITER.¹⁰

A. Experiments and modeling

Enhanced energetic ion transport due to the presence of microinstabilities is well established by basic plasma experiments. Here, the energetic ions feature gyroradii that are much larger than the cross-field scale of the fluctuations (though this is varied in course of the studies, as will be discussed below). These experiments provide excellent diagnostic access as the electron temperatures are typically $T_e \leq 10$ eV, while the energetic ion source is well characterized with beam ion energy $E_b \leq 1000$ eV. These experiments are conducted in both linear and simple toroidal geometry.

Early experiments in a linear device, the LAPD,¹¹ showed that both the energy slowing down and spatial diffusion of energetic ions ($E_b \approx 350$ eV with $T_e \approx 0.2$ eV) are classical.¹² These observations were made in the LAPD afterglow for which the thermal background plasma transport is separately known to be classical¹³ (i.e., there are no pressure gradients or turbulent fluctuations). In order to study energetic ion transport due to turbulence, an experiment¹⁴ was conducted in the main discharge with a copper plate covering half of the cathode in order to create a large pressure gradient. Firing a lithium beam with $E_b = 400 - 1000$ eV into this plasma with $T_e \approx 5$ eV and density fluctuation level $\delta n/n \leq 80\%$ produced beam widening beyond that expected from the classical effects of collisions and beam divergence. This transport enhancement increases as E_b is reduced and the beam ion gyroradius approaches the radial scale length of the fluctuations. Injecting the beam outside of the pressure gradient region produces classical profile spreading. These results motivated additional work¹⁵ in which the beam ions were held fixed while the turbulence scale size and correlation length was changed through variations in plasma species and biasing of the cathode blocking plate. Beam ion turbulent transport was dominated by a gyrocenter drift while the ion energy change was essentially zero. Regimes of subdiffusive and diffusive transport indicate the rich physics involved in this interaction.

A great advance in the understanding of energetic ion interactions with plasma turbulence has been achieved through experiments and modeling of the simple magnetized torus TORPEX.¹⁷ Initial experiments¹⁶ showed that firing lithium ions of $E_b = 300 - 600$ eV ($T_e \approx 5 - 15$ eV) through regions of plasma turbulence, including larger scale structures known as blobs,¹⁸ resulted in broadening of the beam profile beyond classical expectations. The well characterized turbulence of TORPEX encouraged theoretical work that used the experimental parameters for modeling of energetic ion transport at these parameters. Regimes of sub and superdiffusion are identified by a theoretical treatment¹⁹ that combines fluid turbulence simulations with energetic ion orbit following. Superdiffusive transport occurs when the turbulent potential structures are static with respect to the energetic ion motion. Of particular importance for future considerations in tokamak geometry, the energetic ion transport becomes subdiffusive when the particles cross the turbulent structure vertically faster than radially, a process which serves to decorrelate the ion from the turbulent structure and reduce its transport. This led to a Lévy walk description of the energetic ion diffusion²⁰ in which the different transport regimes were characterized according to the ratio of ion energy to plasma temperature, E_b/T_e : $E_b/T_e = 5$ is superdiffusive, $E_b/T_e = 25$ is diffusive, and $E_b/T_e = 250$ is subdiffusive. Describing the effective particle diffusivity in terms of this ratio is a hallmark of theory applicable to tokamaks. A detailed treatment²¹ focusing on interchange mode turbulence within TORPEX parameters reproduces many features observed in the experiment and has motivated additional hardware development (i.e., toroidal position adjustment of the beam) for future comparisons.

While basic plasma devices have conclusively demonstrated the ability of microturbulence to enhance the transport of energetic ions, the experimental evidence from tokamaks overwhelmingly shows that the effect is negligible. These studies include both fusion-produced 3.5 MeV α -particles and energetic ions resulting from NBI and ICRH. Energetic ion diffusivities, D_{EI} , were determined from measurements many times on TFTR.²² It must be noted that these studies, including the theoretical references and the new experiments presented later, use D_{EI} to represent the diffusivity due to unidentified, or anomalous, mechanisms (the term “anomalous diffusivity” is often used to describe turbulence-induced diffusivity). A value of $D_{EI} = 0$ corresponds to transport that is accurately described by the neoclassical effects of collisions and particle drifts. In TFTR, the 1 MeV tritons and 3 MeV protons resulting from deuterium-deuterium (DD) fusion were observed²³ to agree with models setting $D_{EI} = 0$, though measurement uncertainty required an upper bound of $D_{EI} < 0.1$ m²/s. These shots were deemed free of large scale MHD, and they utilized a range of plasma parameters achieved with neutral beam heating powers of $P_{NB} = 5 - 12$ MW. Instances of anomalous fusion product transport and loss were observed,²⁴ but only in plasmas featuring a smaller major radius ($R = 2.45$ m compared to the more typical 2.6 m). This transport enhancement was ubiquitous with the altered shape, including low confinement plasmas and the high confinement “supershots” that featured $P_{NB} = 32$ MW,

and it was determined²⁵ that the transport mechanism could not be related to plasma fluctuations because all fluctuation characteristics varied widely across the range of plasmas observed. Modeling of ripple diffusion in these cases eventually provided²⁶ a qualitatively accurate description of the observations. Fusion α -particle transport was observed²⁷ to follow neoclassical slowing down behavior, where measurements²⁸ extended into the range of $E_b/T_e \geq 18$ (here, $E_b = 150 - 600$ keV is the α -particle energy) and the slowing down time of $\tau_s \approx 0.5$ s provided ample time for transport enhancements to manifest. Throughout the course of experiments at TFTR, some anomalous fusion-product transport was observed in DD plasmas, but not in DT plasmas.²⁹

Beam ion transport was also studied extensively on TFTR. The experimental method involves measuring properties that are sensitive to the beam ion profile and density such as the neutron rate and plasma stored energy. Values for D_{EI} were provided to TRANSP,³⁰ which then modeled the expected plasma response to the enhanced beam ion transport. This work³¹ found instances of $D_{EI} < 0.2$ m²/s across a range of high-power DT shots. Modeling of experiments³² that used only neutron decay following short beam pulses determined core values of $D_{EI} < 0.05$ m²/s. These values of D_{EI} were modeled across the entire plasma profile, which seemed inconsistent with experimental indications that beam ion confinement in the core was much better than that in the outer half of the plasma. Refinements to the modeling were made to allow defining $D_{EI} = D_{EI}(r)$, where r is the plasma minor radius. Later work^{33,34} found that the beam ion transport enhancement was consistent with a large diffusivity increase at the radial position corresponding to the stochastic ripple loss region. These results were applicable across a range of both Ohmic (beam pulses for energetic ion seeding and diagnostics only) and high-power supershots. Remaining cases of anomalous beam ion diffusion are reported³⁵ in reversed shear plasmas. Neutron profiles show that these beam ions are lost, however, and not merely redistributed. It is noted that no significant MHD was observed, though the reversed shear nature of these shots suggests that Alfvén cascades³⁶ may have been present but not detected. While sensitive edge magnetics similar to those available on TFTR have detected cascades previously,³⁷ the most detailed and systematic observations have been made with fast time-resolved interferometers that pass near the center of the plasma.^{38,39}

Results from other tokamaks provide additional examples of either classical transport or initially anomalous energetic ion transport that is eventually explained in terms of non-microturbulence features. Fusion-produced 1 MeV tritons experienced enhanced transport in JT-60U that was determined to be caused by ripple diffusion.⁴⁰ A similar fusion-product study⁴¹ at DIII-D concluded neoclassical transport accurately accounted for measurements across a range of plasmas including the “very high” confinement (VH-mode) shots in which the confinement times were twice as long as in standard H-modes. These experiments also highlight the strong transport effect of MHD; the highest toroidal β values achieved at the time ($\beta_\phi = 11.1\%$) demonstrated that reductions in MHD levels led to measurable improvements in

energetic ion confinement. Anomalous diffusion of tritium beam ions is reported⁴² in JET in the case of reversed shear profiles. In this case, however, the measured plasma parameters are better modeled by using $D_{EI} = 0$ and reducing the beam power (i.e., reducing the number of injected beam ions) than by setting $D_{EI} > 0$ alone. Again, this result is applicable to a range of plasma parameters including low confinement shots. The required beam power reduction is greater than the experimental uncertainty in the beam power, but it is noted that previous campaigns in which the beam-beam neutron component was smaller did not require such power reductions to reproduce experimental observations.

In contrast to the studies referenced above, three recent cases seem to support the concept of measurable beam ion diffusion due to microturbulence. These cases occur during off-axis NBCD scenarios and they are summarized in Ref. 6. ASDEX Upgrade observes⁴³ absolute levels of off-axis NBCD that are smaller than the expected values based on neoclassical theory. The broadened beam ion profile is consistent with $D_{EI} = 0.5$ m²/s, implying a considerable transport mechanism. Off-axis NBCD at DIII-D produced an example^{44,45} of a similar process, with the transport enhancement increasing with P_{NB} (since the beam energies are fixed at $E_b \approx 80$ keV, this corresponds to a decreasing E_b/T_e). A value of $D_{EI}(r) = 0.5\chi_i(r)$, where χ_i is the power-balance computed ion thermal diffusivity, did not reduce the energetic ion density enough to agree with the experimental profile, and further increasing D_{EI} produced greater discrepancy between the measured and simulated profile shapes. Noting that the computed χ_i is typically an order of magnitude larger than the neoclassical χ_i , this is another case demonstrating a very large transport enhancement (D_{EI} peaked at approximately 1 m²/s for $E_b = 40$ keV).⁴⁴ For context, empirical studies at DIII-D found⁴⁶ that a constant $D_{EI} = 0.3$ m²/s is typically sufficient to account for transport of energetic ions due to Alfvén eigenmodes, while recent experiments⁴⁷ showed that neutron rates asymptote to the $D_{EI} = 0$ calculation as AE activity decays away. A separate case investigated the transport enhancement by using on-axis beam injection at reduced energy, $E_b = 58$ keV, along with spectroscopic techniques to show⁴⁸ that beam ion diffusion was larger than neoclassically expected for $E_b \lesssim 30$ keV (plasma temperatures were not reported for that plasma). Finally, JT-60U reported⁴⁹ off-axis NBCD profiles that disagreed with theoretical expectations. While this work concluded that beam ion diffusion is an unlikely explanation for the disagreement, it is still cited as a motivation for investigations into the possible effects of microturbulence on beam ions. A review of these results, in the context of the new observations presented here, will be given in Sec. VI.

B. Theory and simulation

A considerable amount of theoretical and simulation work has been completed in the area of energetic ion transport by microturbulence. In the summary presented below, the energetic ions are treated as passive tracer particles, i.e., they do not drive instabilities due to their own pressure gradients. A rigorous study⁵⁰ concerning the applicability of tracer

particle analysis in determining turbulent transport found that in many cases this is a suitable method (Fick's law must hold for the system). Early work focused on the importance of confining fusion α -particles, with an analytic theory review⁵¹ prioritizing ripple and low- n (toroidal mode number) MHD well ahead of transport due to microturbulence. The work of Ref. 51, now more than 20 years old, described the importance of electromagnetic turbulence over electrostatic for α -particles (a result also determined from more recent work⁵² indicating energetic ion diffusion due to electromagnetic turbulence is invariant with ion energy), though even the electromagnetic contribution, with $D_{EI} \approx 0.062 \text{ m}^2/\text{s}$, is small compared to the transport from MHD. An account of the expected α -particle diffusivity due to MHD (as motivated by the experiments of the time, and using the ITER parameters of the time) showed⁵³ that the α -particle heating efficiency decreased to a possible ignition-preventing level of 95% in the case of $D_{EI} \geq 3.0 \text{ m}^2/\text{s}$. A detailed accounting of those calculations given in a separate work.⁵⁴

Early simulations of particle and energy transport in turbulent fields found⁵⁵ that diffusivity is reduced as the particle gyroradius increases. In later simulation work,^{56,57} it was suggested that the reduction in turbulent diffusion as a function of particle gyroradius could be used to determine the character of the turbulent fluctuations. Tracer particle simulations found⁵⁸ that increasing gyroradius greatly reduces the resultant particle transport, while confirming that the diffusive response to a turbulent field still holds. Other simulations show⁵⁹ that the turbulent diffusion of particles actually increases with gyroradius if the correlation time of the turbulent potential fields is similar to the effective time of flight of the guiding center. This is the drift transport coefficient, however, while the total diffusion coefficient is still reduced compared to thermal particles. Building on this work, other numerical simulations reproduced⁶⁰ the key features and stated that fusion α -particles will likely suffer from significant turbulent transport because the turbulence correlation lengths will be comparable to the α -gyroradius.

The continued advancement of gyrokinetics and its associated computing framework have allowed it to extend beyond thermal plasma transport. The gyrokinetic formulation was rederived⁶¹ with consideration for the effects of highly energetic ions. The suprathermal component was limited to the field-parallel velocity term, with the perpendicular energy set equal to T_e . Turbulent diffusivity of energetic ions peaked at energies for which the particles' curvature drift velocity matched the diamagnetic drift velocity of the turbulence. The largest transport effects were seen at comparatively low energies, $E_b \lesssim 3T_e$. GYRO⁶² simulations demonstrated⁶³ that α -particles will suffer transport due to microturbulence in ITER. Simulations using the GENE⁶⁴ code identified⁶⁵ a complex interplay between different parameters, including effects due to poloidal drifts. That work noted significant turbulent transport of energetic ions should occur when the particle gyroradius is comparable or smaller than the turbulence correlation length. Subsequent simulations⁶⁶ provided a detailed discussion of energetic ion orbit averaging and turbulence decorrelation physics and used ITER parameters to show a large Kubo number (defined in

Ref. 43 as $K = V_{E \times B} \tau_c / \lambda_c$, where $V_{E \times B} = 900 \text{ m/s}$ is the $E \times B$ velocity, $\tau_c = 1.8 \times 10^{-4} \text{ s}$ is the turbulence correlation time, and $\lambda_c = 1.6 \text{ cm}$ is the turbulence correlation length) of $K = 10$, which is large enough for a transport enhancement to manifest.

Simulations with the particle-in-cell code GTC⁶⁷ identified^{68,69} scalings of the energetic ion diffusivity in the presence of ion temperature gradient (ITG) type turbulence. For passing energetic ions, this goes as $D_{EI, \text{pass}} \propto T_e/E_b$, while for trapped ions, the relationship is $D_{EI, \text{trap}} \propto (T_e/E_b)^2$. Other simulations with GENE identified⁵² the same dependence for passing ions, but differed in the trapped dependence with $D_{EI, \text{trap}} \propto (T_e/E_b)^{3/2}$. The difference in trapped ion response stems from calculations of orbit averaging and decorrelation with turbulent potential structure, a subject that is in ongoing debate.^{70,71} Simulations focusing on trapped electron mode (TEM) type turbulence reproduced⁷² $D_{EI, \text{trap}} \propto (T_e/E_b)^2$, and, together with ITG-type simulations,⁷³ identified that the diffusive/subdiffusive behavior is dictated by machine size. Recent GYRO simulations⁷⁴ indicate a stronger falloff for both passing ions, $(T_e/E_b)^{3/2}$, and trapped ions, $(T_e/E_b)^{5/2}$. The effects of zonal flows have been studied,⁷⁵ and the results indicated an increase in poloidal diffusion of energetic ions, with a simultaneous decrease in radial diffusion. Many of these simulations treat the energetic ion population as an extra hot Maxwellian, which has been shown⁷⁶ to produce results that are consistent with simulations employing the more realistic slowing down distribution.

A large set of ITER-relevant modeling and simulation with GENE has found^{77,78} values of $D_{EI} > 0.1 \text{ m}^2/\text{s}$ through the MeV ion energy range. Later work⁷⁹ reviewed NBI ($E_b = 1 \text{ MeV}$) in ITER and determined that expected NBCD profile modification was minimal. It is worth noting that work considered fractional beam energy components ($E_b/2$ and $E_b/3$) that arise in standard neutral beams from molecular deuterium,⁸⁰ but MeV beams in ITER will use negative neutral sources⁸¹ that produce only the full energy component. The inclusion of lower energy beam ions should tend to increase the modeled effect of turbulence-induced diffusion. If the beam energy is lowered to 300 keV and moved to $\rho = \sqrt{\psi_t/\psi_i(a)} = 0.5$ (where ψ_t is the toroidal magnetic flux and a is the minor radius) resulting in $E_b/T_e = 20$, then changes in the NBCD profile were observed on the order of 5%. Predictions⁸² for energetic ion transport due to turbulence in DEMO⁸³ and TCV⁸⁴ suggest new regimes that might provide strong experimental evidence for the effect. The TCV scenario depends on the completion of a neutral beam upgrade.⁸⁵ The most thorough and complete investigation of this transport mechanism for burning plasmas is contained in the thesis of Albergante.⁸⁶ The most recent work⁸⁷ on this topic provides analytic expressions for expected D_{EI} in terms of experimentally accessible parameters. These expressions are used in the modeling performed for the present experiments.

III. EXPERIMENTAL SETUP

A. Typical plasma parameters and NBI

A series of low confinement mode (L-mode) plasmas are presented in this paper. The time evolution of one such

shot is shown in Fig. 1, and is representative of the qualitative behavior of the plasmas in general. On-axis beam injection during the current ramp drives Alfvén eigenmodes,⁸⁸ which must be avoided due to their significant transport effect on beam ions. A steady electron density [from interferometry,⁸⁹ Fig. 1(a)] and central temperature [from electron cyclotron emission,⁹⁰ Fig. 1(b)] are maintained after reaching flattop [Fig. 1(c)]. The neutron rate⁹¹ [Fig. 1(d)] is modulated according to the injected P_{NB} [Fig. 1(e)]. Off-axis NBI replaces the on-axis beams during the flattop and is maintained for multiple beam ion slowing down times. The total injected beam power remains constant (below 5 MW in all shots) and $\beta_N \leq 0.56$. The MHD-quiescent period, indicated as the shaded region in Fig. 1, occurs before the appearance of sawteeth. Characteristics of the turbulent fluctuations are presented within the analysis of particular shots.

In order to inject $P_{\text{NB}} \geq 4$ MW while avoiding confinement transitions, the plasmas are operated in the unfavorable $\vec{\nabla}B$ -drift direction. Figure 2 shows the equilibrium shape for shot 145183 at $t = 1585$ ms. The last closed flux surface (solid blue line) and the mid-radius position of $\rho = 0.5$ are shown. The color contour represents the birth pitch (v_{\parallel}/v , where v_{\parallel} is the particle velocity along the magnetic field and v is the total velocity, though the sign of v_{\parallel} is determined according to the plasma current) of the off-axis injected neutral particles. This beam ion birth profile is calculated with NUBEAM (Sec. III C). Performance of the off-axis beams is extensively studied and NUBEAM modeling of the injection is validated, where initial discrepancies appear related to uncertainties in beam power,⁹² but not anomalous transport mechanisms.

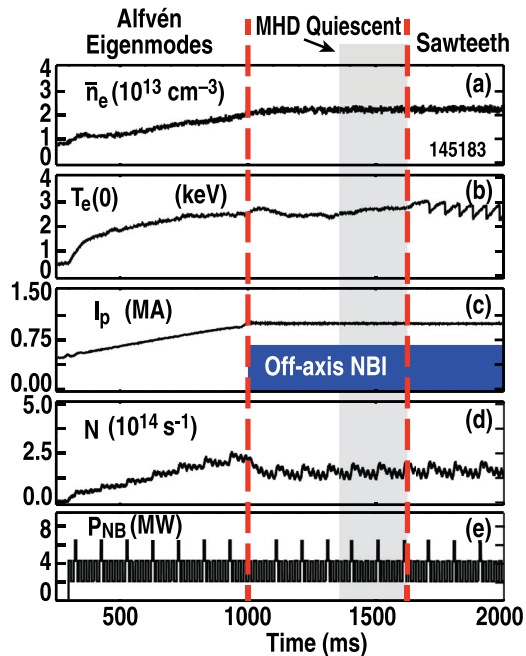


FIG. 1. Time evolution of plasma parameters from shot 145183 indicating the regions of energetic ion transport mechanisms and the presence of off-axis NBI. (a) Line-averaged density, (b) central electron temperature, (c) plasma current, (d) neutron rate, and (e) neutral beam power.

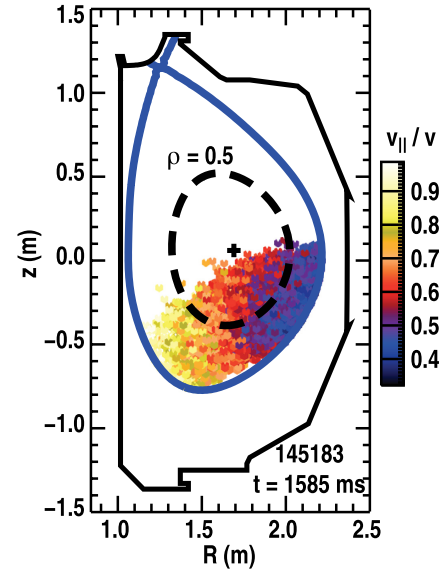


FIG. 2. Magnetic equilibrium from shot 145183 at $t = 1585$ ms. Color contour represents the birth pitch of off-axis injected neutral beam particles.

B. Measurements of turbulence and energetic ion transport

The primary energetic ion diagnostic is the fast ion D_{α} (FIDA) system,⁹³ which is a spectroscopic measurement enabled by charge exchange between energetic ions and injected neutrals. The charge exchange process results in a favorable situation of excited-state fast neutrals that then emit Doppler shifted photons, providing a spatially localized signal with energy resolution of the energetic ion profile.⁹⁴ Each FIDA chord, with its associated viewing geometry, features a unique sensitivity across the phase space of the energetic ion distribution.⁹⁵ Figure 3 provides an example of one such phase space weighting for the $R = 1.97$ m chord during $t = 1585$ ms in shot 145183. This calculation convolves the diagnostic viewing geometry with the charge-exchange probability and the energetic ion distribution (calculated with $D_{\text{EI}} = 0$). The contour indicates the contribution of different parts of the energetic ion distribution to the FIDA signal, i.e., the integral over this contour is 100%. The dominant region of the distribution, in this example, is $E_b > 40$ keV and $v_{\parallel}/v > 0.5$. The overlaid lines represent the trapped/passing

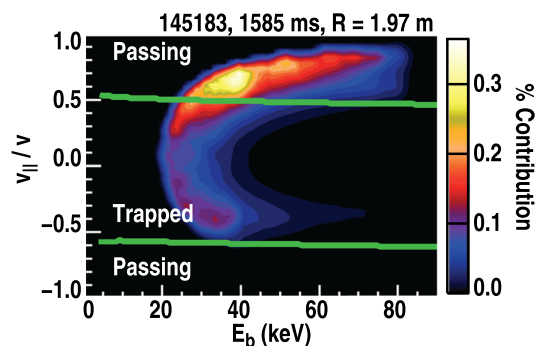


FIG. 3. Phase space weighting of the FIDA chord at $R = 1.97$ m in shot 145183.

boundary as determined with the constants-of-motion orbit code described in Ref. 47. Passing ions, which are responsible for driving current, make the largest contribution to this FIDA signal. A thorough treatment of this type of phase space weighting is given in Ref. 96, where those results for a collective Thomson scattering diagnostic translate directly to FIDA systems. Of relevance to the present investigation, it is noted that early FIDA diagnostic development demonstrated⁹⁷ that measured energetic ion profiles were classical across a range of MHD-quiet plasmas (including variations in plasma conditions and beam power). A view of typical radial positions for a variety of diagnostics is shown in Fig. 4. Turbulent fluctuations are measured by multiple systems. Beam emission spectroscopy (BES)⁹⁸ measures electron density fluctuations, thereby providing \tilde{n}_e/n_e , and turbulence correlation lengths. BES is sensitive to the wavenumber range $k_\theta \rho_s < 0.5$, where k_θ is the poloidal wavenumber and ρ_s is the thermal ion sound gyroradius. The Doppler backscattering system (DBS)⁹⁹ measures density fluctuations and the velocity of turbulent structures through an intermediate range of $k_\theta \rho_s < 2$. Electron temperature fluctuations are documented by the correlation electron cyclotron emission system (CECE)¹⁰⁰ with sensitivity of $k_\theta \rho_s < 0.3$. The CECE diagnostic is coupled with an X-mode reflectometer that measures density fluctuations within the same sampling volume. This combination allows for determination of the coherency and phase angle between density and temperature fluctuations.^{101,102}

C. Beam ion modeling

The NUBEAM^{103,104} module of TRANSP is used to simulate neutral beam injection in the DIII-D shots described here. NUBEAM is a Monte Carlo code that incorporates the

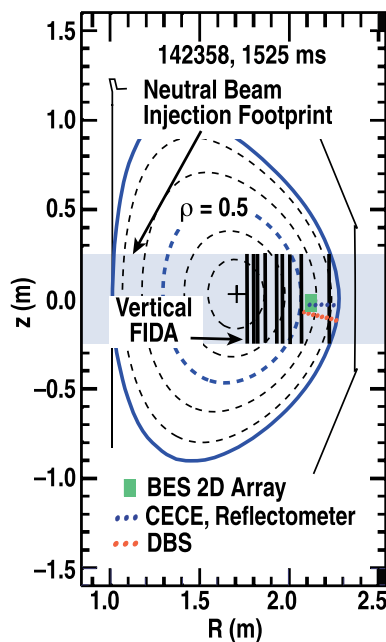


FIG. 4. Magnetic equilibrium from shot 142358 at $t = 1525$ ms showing typical positions of the FIDA (vertical black lines), BES (green rectangle), CECE/reflectometer (blue ovals), and DBS (red ovals) views.

beam geometry and injected power, along with measured plasma profiles, to calculate beam ionization profiles and subsequent beam ion slowing down. Experiments have verified⁴⁵ NUBEAM's ability to accurately describe the beam ion population (the anomalous examples^{44,45,48} are discussed in Sec. VI). The beam ion distribution, $F_b = F_b(E_b, v_{\parallel}/v)$ calculated by NUBEAM is passed to the synthetic diagnostic code FIDASIM¹⁰⁵ to simulate the expected FIDA signals. The distribution is calculated with neoclassical transport effects by default, and an additional diffusivity may be provided to simulate enhanced transport regimes (e.g., due to coherent MHD or microturbulence). This anomalous diffusivity can be provided as $D_{EI} = D_{EI}(E_b, v_{\parallel}/v, \rho, t)$, where the pitch dependence is coarse grained into six categories of trapped or passing topology. As this is a Monte Carlo code, care is taken to ensure that a sufficient number of ions are modeled in order to provide suitable input to FIDASIM. Earlier work³¹ with the Monte Carlo beam ion modules of TRANSP reported a noise level of 5%. Figure 5 presents $F_b V$ contours, where V is the local Monte Carlo zone volume, for three different settings of the number of followed ions in NUBEAM. These distributions from shot 145183 are averaged over a short time period of 20 ms centered on $t = 1585$ ms. The distribution computed by following 10^6 particles as shown in Fig. 5(a) is noticeably smoother than the one with 10^4 particles shown in Fig. 5(c). All FIDASIM simulations are performed using F_b from NUBEAM

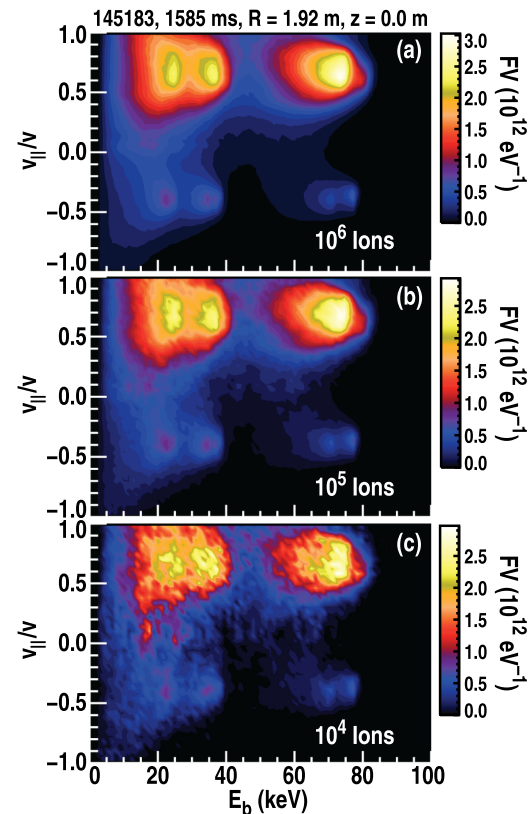


FIG. 5. Beam ion distributions calculated by NUBEAM with varying number of ions followed: (a) 10^6 , (b) 10^5 , and (c) 10^4 .

calculations using at least 10^5 particles, and an example F_b is shown in Fig. 5(b).

IV. RESULTS DURING OFF-AXIS NBCD

Off-axis NBI is investigated due to its particular relevance for ITER, in which all of the heating and current drive beams will be off-axis (e.g., a modeled beam ion profile peaked at $\rho \approx 0.2$ is shown in Ref. 106). Since beam ions are injected across the mid-radius of the plasma in this mode of operation, it may be expected that diffusion due to microturbulence constitutes an important transport effect. The time evolution of off-axis NBI shot 145183 is shown in Fig. 1. Off-axis NBI begins at the current flattop and is maintained for a short time period before the time region of analysis. This shot features $P_{\text{NB}} = 2.1$ MW of off-axis injection with a deposition profile as shown in Fig. 2. Radial profiles are presented in Fig. 6, including electron density [Fig. 6(a)], electron and ion temperatures [Fig. 6(b)], and toroidal rotation [Fig. 6(c)]. These data are collected by Thomson scattering,¹⁰⁷ electron cyclotron emission (ECE), and charge-exchange emission spectroscopy (CER).¹⁰⁸ Solid lines represent the best-fit splines to the individual measurements, and the resulting reduced- χ^2 (hereafter written χ_{red}^2) is indicated. Electron and ion temperatures are similar across the profile, with T_e surpassing T_i in the center of the plasma. For context with the existing theoretical scalings, this shot features $E_b/T_e(0) \approx 30$ during the period of interest. Significant fluctuation levels due to background microturbulence are

observed. Figure 7 plots power spectra of electron temperature fluctuations in which the fluctuation level approaches $\delta T_e/T_e \approx 1\%$. Density fluctuations are observed with comparable spectra and slightly lower amplitude. The neutral beam viewed by the BES system is the one that tilts to provide off-axis injection, which limits the innermost radial position for which plasma density fluctuations can be measured.

Energetic ion diffusion due to microturbulence is modeled with two independent methods in this shot. In each case, these models produce values of D_{EI} that are passed to NUBEAM. One method uses the newly developed code DEP.⁷⁴ DEP is a quasilinear model in which the ratio of energetic ion turbulent diffusivity matrix elements to χ_i is calculated in radial and velocity space. Only matrix elements for radial diffusion driven by radial gradients are used, i.e., velocity gradients are ignored. For modeling, the values of D_{EI} are determined by

$$D_{\text{EI}}(E_b, \Lambda) = \left(\frac{D_{\text{EP}}}{\chi_i} \right)_{\text{th}} \chi_{i,\text{ex}}, \quad (1)$$

where Λ indicates that the D_{EI} values are separated into trapped and passing components, the ratio D_{EP}/χ_i is the theoretical value calculated by DEP, and $\chi_{i,\text{ex}}$ is the experimentally determined thermal ion heat diffusivity (e.g., from power balance analysis in TRANSP). The TGLF¹⁰⁹ code determines the linear frequencies, growth rates, and nonlinear spectral weights for the turbulent modes based on the measured plasma profiles, and passes them to DEP for calculation of D_{EP}/χ_i . TGLF is able to resolve ion modes (e.g., ITG, which is dominant in this off-axis case), and electron modes (e.g., TEM, which is dominant across much of the plasma in the on-axis case of Sec. V). Both TGLF and DEP are integrated into TRANSP/NUBEAM, providing the ability to self-consistently account for the energetic ion transport effect of microturbulence throughout the evolution of a shot.

The second method incorporates the analytic expressions for D_{EI} as determined by Ref. 87, hereafter referred to as the Pueschel model, where Eqs. (12) and (13) are implemented in the present study as

$$D_{\text{EI,pass}} = \frac{0.292 \chi_{\text{eff}}}{(v_{\parallel}/v)^2} \left(\frac{T_e}{E_b} \right), \quad (2)$$

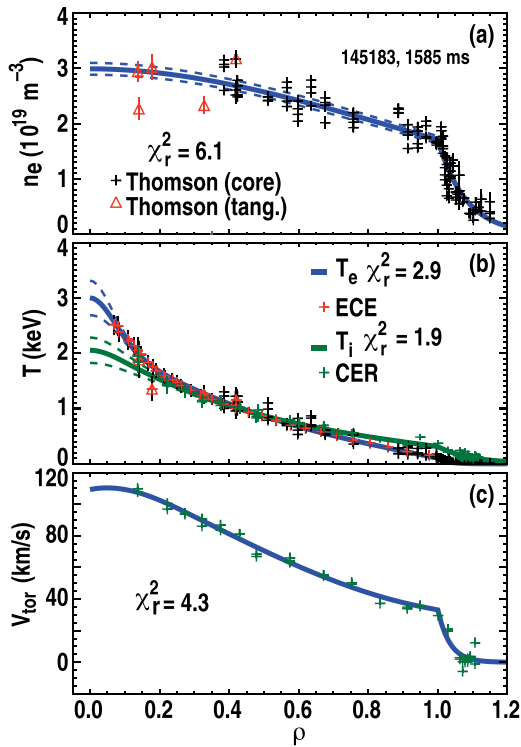


FIG. 6. Plasma profiles from shot 145183 indicating the individual measurements along with best-fit splines (solid lines) and statistical uncertainty range (dashed lines). Profiles are shown for (a) electron density, (b) electron and ion temperature, and (c) toroidal rotation.

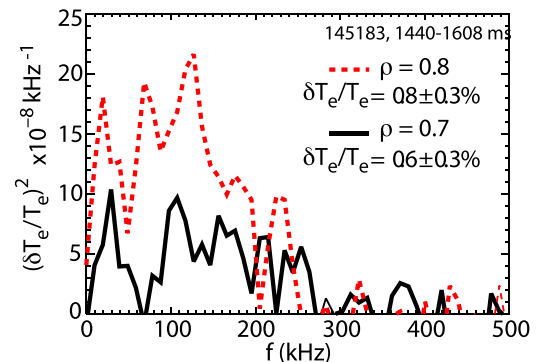


FIG. 7. Spectra of electron temperature fluctuations in shot 145183.

$$D_{\text{EI,trap}} = \frac{0.527 \chi_{\text{eff}} \sqrt{\epsilon}}{(v_{\parallel}/v)[1 - (v_{\parallel}/v)^2]} \left(\frac{T_e}{E_b} \right)^{3/2}, \quad (3)$$

where these represent the diffusivity due to electrostatic turbulence, $\chi_{\text{eff}} = \chi_e + \chi_i$ is the effective thermal diffusivity determined by adding the ion and electron contributions, and $\epsilon = r/R_o$ is the inverse aspect ratio with R_o the tokamak major radius (the original work⁸⁷ notes that these expressions are meant as approximations to enable systematic studies, so the “=” here represents the fact that these are the exact expressions used to generate D_{EI} input for NUBEAM). The Pueschel values are calculated using $v_{\parallel}/v = 0.66$ for the passing ions and $v_{\parallel}/v = 0.2$ for the trapped ions. These values are representative for the DIII-D beam injection cases. The resulting D_{EI} during the time of interest from these two methods are shown in Fig. 8. Diffusivities for the passing ions are given in Figs. 8(a) and 8(c). Both D_{EI} profiles peak near $\rho = 0.6$, with the DEP values generally larger than the Pueschel values and exhibiting a faster rolloff with energy. Figures 8(b) and 8(d) illustrate the anomalous diffusivities for the trapped population. The results for the trapped ions are comparable between the two methods.

All measured energetic ion properties indicate that the transport is classical in this shot. In some cases, modeling based on the energetic ion diffusion enhancement from microturbulence shows that the effects are too small to uniquely resolve compared to the classical values. A FIDA spectrum from the chord centered at $R = 1.76$ m is shown in Fig. 9(a). The solid line is the experimentally measured spectrum, while the dashed line represents the classically expected value from FIDASIM. A representative error bar is plotted on the measured spectrum, where this represents the statistical uncertainty. Systematic uncertainties are treated in the FIDA density profiles to follow. For the spectrum, Fig. 9(a) highlights the FIDA density integration region of $20 \leq E_{\lambda} \leq 40$ keV, where E_{λ} is the Doppler shift energy corresponding to a given wavelength. This range is motivated by the observed presence of an energetic ion tail. The inset plots the measured spectra on a semi-log format in which the

energetic tail appears as a linear region (the dotted line is a guide for the eye). It is seen that the tail occurs at Doppler shifts corresponding to wavelengths below 654 nm. The FIDA contribution at Doppler shifts below 20 keV is poorly resolved because of the large light signals from thermal D_{α} . The FIDA density, which is calculated by integrating the spectrum and dividing out the radial profile of neutral density due to the injected active-spectroscopy beam source, is given in Fig. 9(b). The +-symbols represent the measured values, and the remaining traces represent the expected profile based on either classical or turbulent transport models. The ribbon about the classical profile represents the 25% uncertainty in FIDASIM. The measured profile is a good fit to the +25% edge of the classical profile. These results are obtained entirely independent of one another, i.e., there is no normalization applied within this analysis. In fact, the investigation of possible transport by microturbulence requires that normalizations be avoided since turbulent fluctuations remain present even in otherwise quiescent plasma conditions. Error bars on the measured profile points represent the statistical error, which does not account for systematic uncertainties. In order to consider systematic uncertainty, we find the scaling factor (applied to the measured profile) that produces the lowest value of χ_{red}^2 . This amounts to assuming that the *shape* of the classical synthetic result is more rigidly accurate than the absolute value of the radiance. For the profile shown in Fig. 9(b), a scaling factor of 0.8 produces the minimum value of $\chi_{\text{red}}^2 = 12.2$. This χ_{red}^2 is approximately half the value of the equivalent result performed in the presence of Alfvén eigenmodes (treated in Sec. V).

Processing the FIDA measurements in terms of profile fitting also avoids possible quantitative issues with FIDASIM, as discussed in the context of the FIDA profile shown in Fig. 10. The FIDA brightness profile of Fig. 10 is calculated based on measurements from the main-ion D_{α} diagnostic system,¹¹⁰ which measures the entire D_{α} spectrum. The displayed profile, though determined with different analysis techniques, represents the energetic ion density through the observed phase space of the diagnostic just as in the FIDA density plot of Fig. 9(b). In Fig. 10, the

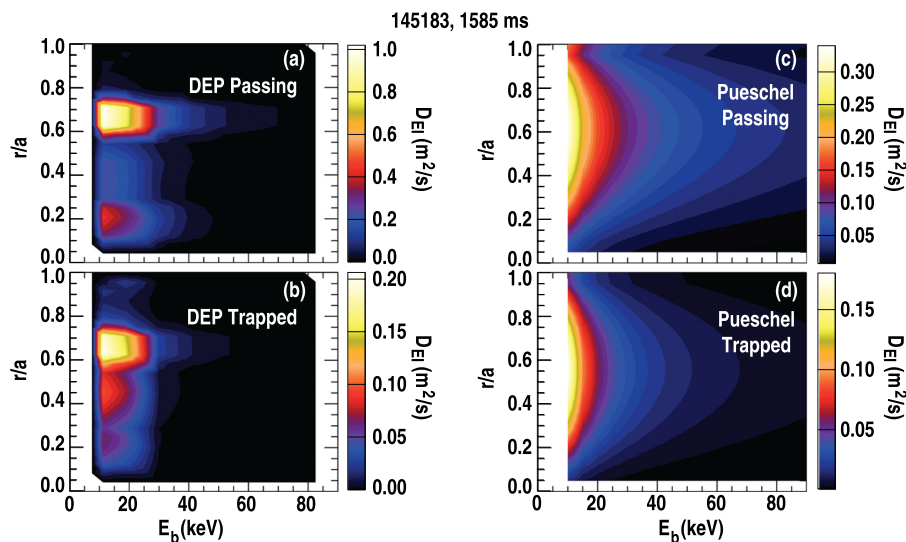


FIG. 8. Values of energetic ion anomalous diffusivity, D_{EI} , as calculated by the DEP code for (a) passing and (b) trapped ions, and by the analytic Pueschel expressions for (c) passing and (d) trapped ions.

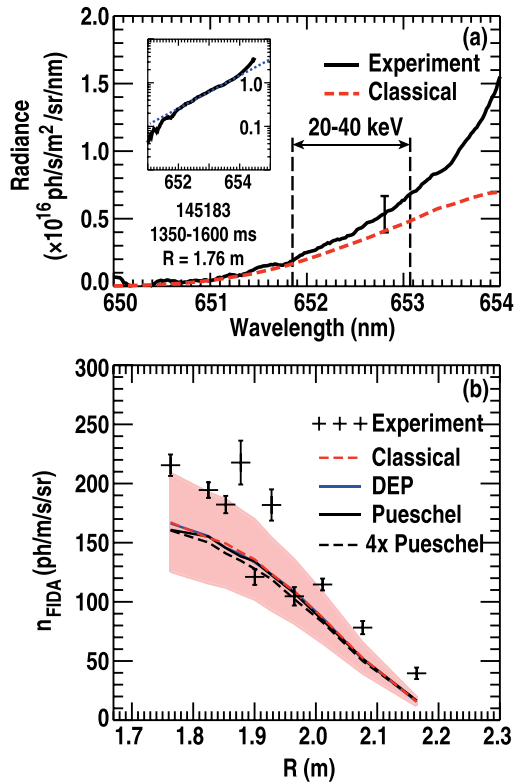


FIG. 9. (a) FIDA spectrum from shot 145183 during the MHD-quiescent period. The experimental spectrum (black trace) is shown with a representative error bar. The classical spectrum (red dashed trace) and the boundaries of the FIDA density integration region are indicated. The inset plot is the experimental data on a semi-log scale to highlight the energetic ion tail (linear portion of plot parallel to dotted blue line). (b) FIDA density as measured (+-symbols) and as expected from classical and turbulent transport models (lines).

experimentally measured profile is seen to be considerably larger than the classically expected profile. The best-fit is achieved by a data scaling factor of 0.65, which produces $\chi_{\text{red}}^2 = 7.5$ and matches the classical shape. The reason for

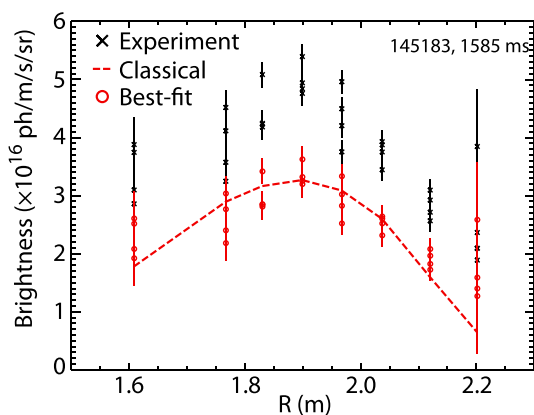


FIG. 10. FIDA brightness profile from the main ion D_x system during off-axis beam injection in shot 145183. The \times -symbols represent the absolutely measured brightness, while the \circ -symbols represent the measured data after being scaled to produce the best-fit to the simulated profile (represented by the dashed line).

FIDASIM under-prediction compared to measured signals is presently under investigation, though initial review¹¹¹ suggests that possible modifications to the calculation of halo light may resolve the issue. Calculated emission due to the halo contribution dominantly adjusts the amplitude of the FIDA profiles, with less effect on their shape. The profile fitting method employed in this analysis is intended to maintain the applicability of these results even in the case of modifications to the synthetic diagnostic code. A summary of the profile results across all of the studied shots is presented in Sec. VIA.

V. RESULTS DURING ON-AXIS NBI

Plasmas with on-axis NBI provide an opportunity to probe conditions (e.g., $E_b/T_e(0) \leq 10$) in which energetic ion diffusion due to microturbulence is theoretically expected. In addition, radial beam ion diffusion occurs always in the outward direction for these centrally peaked energetic ion profiles, which may increase any profile flattening. The magnetic equilibrium for the on-axis NBI shots is shown in Fig. 4. It is not possible to obtain FIDA, BES, ion temperature, and plasma rotation profile data simultaneously given the constraint on the total beam power (2.5 MW), therefore, the results presented here involve different measurements during repeat shots. These are L-mode plasmas ($B_t = 2.06$ T and $I_p = 1$ MA) in which the ratio E_b/T_e is lowered by holding beam energy fixed ($E_b \approx 80$ keV) and increasing T_e roughly a factor of two using electron cyclotron heating (ECH) deposited at $\rho = 0.2$. This results in one set of measurements for the condition of $E_b/T_e(0) \approx 10$ and another set at $E_b/T_e(0) \approx 22$. The time evolution of these paired and repeated shots is shown in Fig. 11, indicating the well-matched behavior. The higher value of E_b/T_e is achieved in shots 142358 and 142380, while the lower ratio is achieved in 142371 and 142381. Radial profiles for these shots, during the MHD-quiescent period of analysis, are shown in Fig. 12. Applied ECH in shot 142371 produces significantly higher electron temperatures [Fig. 12(a)], while the ion temperature and electron density varies little [Figs. 12(b) and 12(c)]. The toroidal rotation profiles are shown in Fig. 12(d), where the dashed lines represent the statistical uncertainty range (in the other plots this range is very small, so those dashed lines are removed for clarity).

The turbulence is well characterized in these plasmas. Figure 13 shows the measurable fluctuation amplitude profiles for density [Fig. 13(a)] and temperature [Fig. 13(b)]. While the density fluctuation amplitude is the same in both cases and peaking near $\tilde{n}/n = 1\%$, the electron temperature fluctuations increase by nearly a factor of two in the lower E_b/T_e case. The temperature fluctuation increase is consistent with a transition from ITG-dominated turbulence (in the higher E_b/T_e case without ECH) to TEM-dominated turbulence (in the lower E_b/T_e case employing ECH to raise the value of T_e/T_i).¹¹² The error bars in Fig. 13(b) represent statistical uncertainty, while the sensitivity limit is equivalent to the reported uncertainty of the temperature fluctuations noted in Fig. 7. Further evidence for the difference in microturbulence character between these cases is given by the

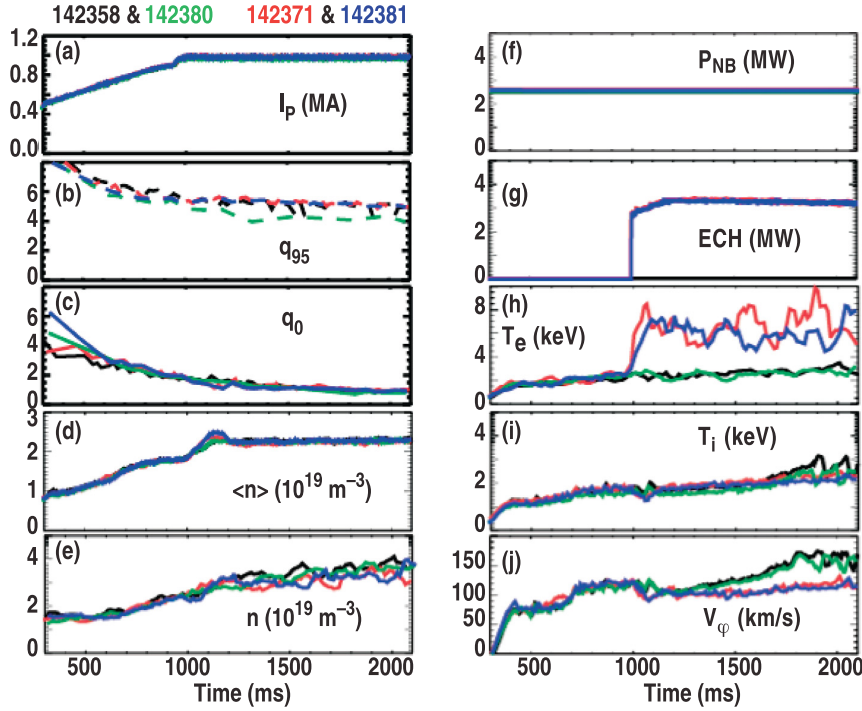


FIG. 11. Time evolution of plasma parameters from the matched shot pairs of 142358 and 142380 and 142371 and 142381. Displayed parameters are: (a) plasma current, (b) q_{95} , (c) central q -value, (d) line-averaged electron density, (e) central density, (f) neutral beam power, (g) electron cyclotron heating power, (h) central electron temperature, (i) central ion temperature, and (j) central toroidal rotation velocity.

cross-phase angle between the density and temperature fluctuations, Θ_{nT_e} , shown in Fig. 14. The measured cross-phase angle is indicated by the darker lines, while the lighter portions of the trace indicate frequencies for which the density/temperature fluctuation coherency is too small to accurately resolve Θ_{nT_e} . In the higher E_b/T_e case of Fig. 14(a), $\Theta_{nT_e} \approx -150^\circ$, while in the lower E_b/T_e case of Fig. 14(b), the value is $-100^\circ \leq \Theta_{nT_e} \leq -50^\circ$. These values are accurately reproduced by GYRO simulations that are plotted as dashed-dotted lines, which further indicates that the turbulent electron heat transport is approximately five

times larger in the lower E_b/T_e case. Detailed analysis and simulation of the microturbulence in these paired shots is given in Ref. 112. TGLF is used to calculate the real frequency of the most unstable mode, which is shown in Fig. 15, indicating that the lower E_b/T_e has a larger region dominated by electron mode turbulence, while the higher E_b/T_e case has a larger region dominated by ion mode turbulence. The radial correlation length of the turbulence is determined using BES measurements of density fluctuations and found to be $\lambda_c(\rho = 0.65) > 2$ cm in both cases. Across the pitch angle and energy ranges of energetic ions in these

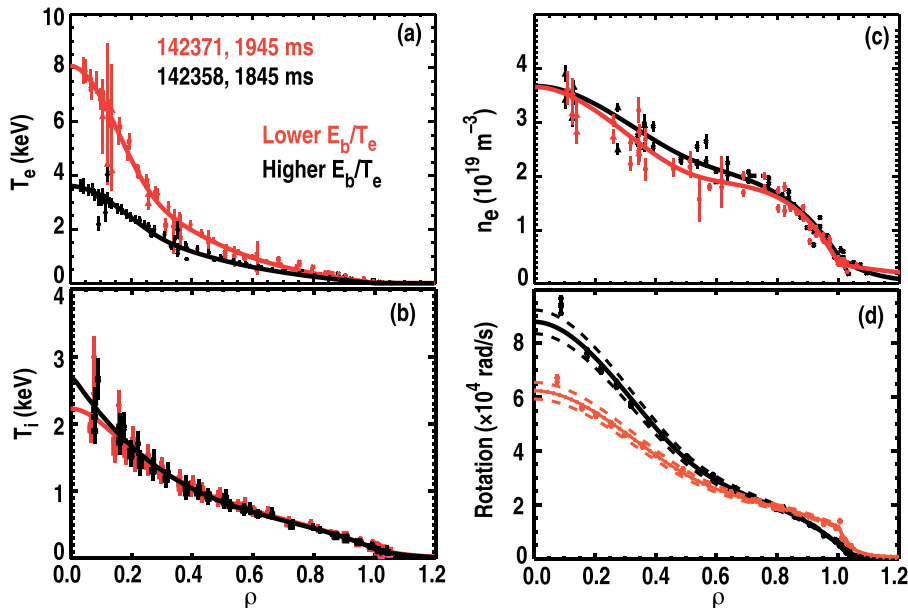


FIG. 12. Radial profiles from the MHD-quietest period of the on-axis NBI shots. Profiles include: (a) electron temperature, (b) ion temperature, (c) electron density, and (d) toroidal rotation.

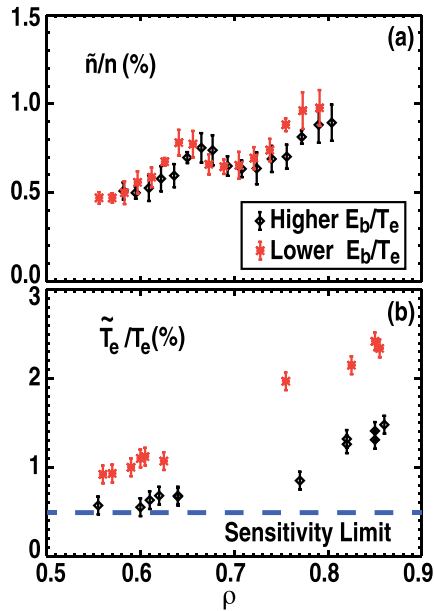


FIG. 13. Profiles of turbulent fluctuation levels measured in the low and high E_b/T_e paired plasmas. (a) Long wavelength density fluctuations measured with BES. (b) Long wavelength electron temperature fluctuations measured with CECE show a factor of two increase between these cases.

$B_t = 2.06$ T plasmas, this radial length can be comparable to the energetic ion gyroradius.

Energetic ion profiles for the higher E_b/T_e case are shown in Fig. 16. These FIDA density profiles are calculated over the energy range $E_\lambda = 20 - 40$ keV. Expected profiles based on classical transport, and calculated with the FIDASIM synthetic diagnostic, are indicated by the dashed lines and ensuing uncertainty ribbons. In Fig. 16(a), the

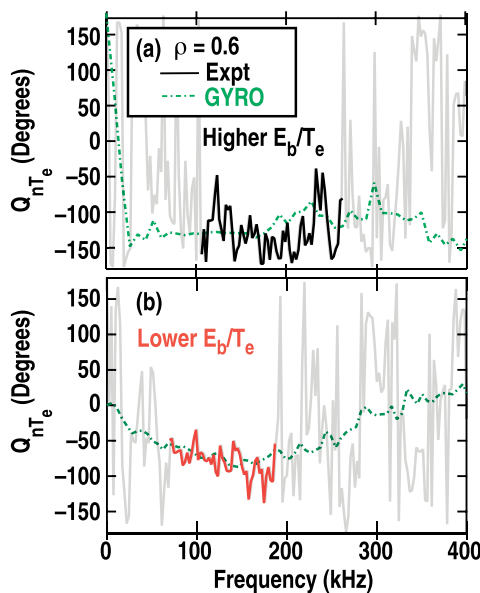


FIG. 14. Cross-phase angle between density and temperature fluctuations in the (a) higher E_b/T_e and (b) lower E_b/T_e cases. GYRO calculated values are given by the green dashed-dotted trace, while the experimental values are indicated by the dark lines (the lighter lines represent frequencies for which the coherency between the signals is too low to resolve the cross-phase angle).

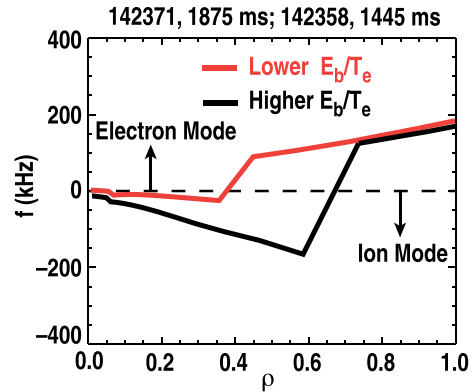


FIG. 15. Real frequency of the most unstable mode as calculated by TGLF for $k_\theta \rho_s = 0.4$. Positive frequencies correspond to electron modes, and negative frequencies correspond to ion modes.

profiles are taken from the plasma current ramp during which Alfvén eigenmodes were observed. Scaling the measured profile by 1.8 produces the minimum $\chi_{red}^2 = 21.8$. This value is $\approx 2 - 20$ times as large as those values determined for all of the profile comparisons made during MHD-quietest time periods when microturbulence is expected to be the dominant transport mechanism. In contrast to the Alfvénic time period, the classical and experimental profiles of the MHD-quietest period in Fig. 16(b) agree very well. Here, a scaling factor of 1.15 produces $\chi_{red}^2 = 1.2$.

It is interesting to note that the on-axis NBI cases produce a spatial profile of energetic ions and microturbulence similar to that in ITER. As shown in Fig. 14 of Ref. 63, the

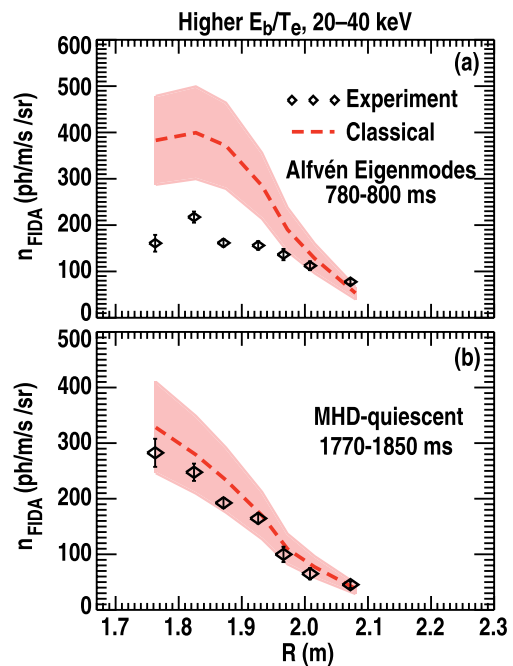


FIG. 16. FIDA density profiles from the higher E_b/T_e cases for (a) an early time during which Alfvén eigenmodes are present, and (b) during the MHD-quietest period. The red dashed lines represent the classically expected FIDA density as computed by the synthetic diagnostic FIDASIM. The uncertainty ribbon about the simulation trace represents a 25% range.

α -particle profile in ITER is expected to be core-localized. Microturbulence, driven by pressure gradients, begins to reach appreciable fluctuation amplitude near mid-radius, and then peaks further out towards the edge. The result is that only for the region $\rho \approx 0.5$ is there both a sizable α -particle density and large amplitude turbulent fluctuations. Figure 17 reproduces this situation using measurements and calculations from the higher E_b/T_e case. On-axis NBI is core-localized as indicated by the FIDA density profile [taken from Fig. 16(b)]. The growth rate of the most unstable turbulent mode is calculated by TGLF and plotted as the dashed line. This scenario should be favorable to measuring a turbulent transport effect because any enhanced diffusion should serve to move energetic ions out of the plasma center. Our results indicate that turbulent diffusion is below an observable limit in this scenario.

The lower $E_b/T_e \approx 10$ case results in comparatively large values of D_{EI} , as shown in Fig. 18. Figure 18(a) shows that $D_{EI} > 0.2 \text{ m}^2/\text{s}$ is achieved up through $E_b \approx 60 \text{ keV}$. The radial distribution peaks nearer to the plasma center compared to the off-axis NBI case discussed in Sec. IV. The trapped ion D_{EI} exhibits a similar radial profile, but is nearly a factor of two smaller than the passing component for all energies. These levels of diffusion lead to a large modeled redistribution of energetic ions. Figure 19(a) plots the NUBEAM-modeled energetic ion density for both the classical and Pueschel treatments. The large values of D_{EI} for $\rho > 0.1$ in the Pueschel formulation result in a significant depletion of energetic ions in the plasma center. This transport is large enough to affect the beam current drive profile as shown in Fig. 19(b). Integrating over this profile indicates that the total beam-driven current of the Pueschel case (133.6 kA) is 11% smaller than the classical expectation (150.7 kA). This is a unique result, as on-axis beam injection modeling⁴³ in ASDEX Upgrade produced no change in beam-driven current profiles when setting $D_{EI} = 0.5 \text{ m}^2/\text{s}$.

FIDA measurements from this case are shown in Fig. 20. The E_λ range for FIDA analysis is determined by review of the individual spectra that are plotted in Fig. 20(a). Lower Doppler shifted energies are resolved in this shot, and the vertical dashed lines mark the values of $E_\lambda = 14.7$ and 40.0 keV . This wide range of analysis should provide a better opportunity to identify transport due to microturbulence

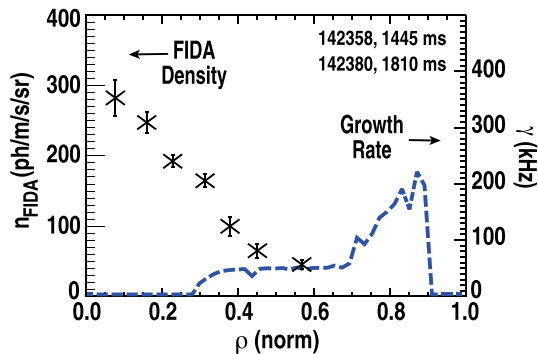


FIG. 17. FIDA density (\times -symbols) and growth rate of the most unstable mode (dashed trace) for the DIII-D on-axis NBI case.

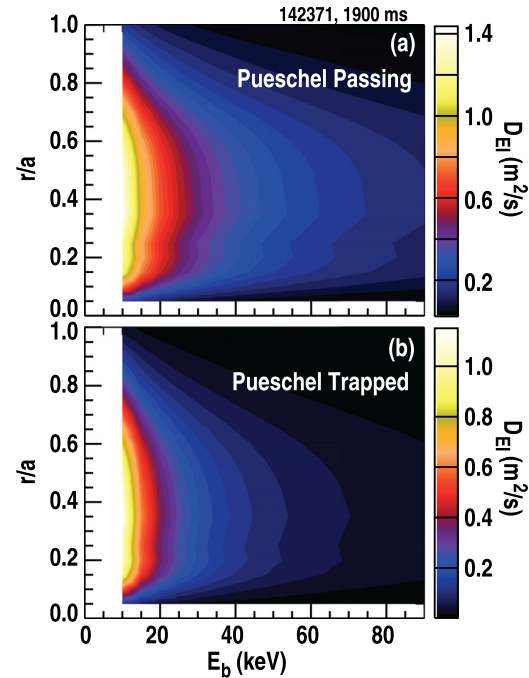


FIG. 18. Values of D_{EI} calculated using the Pueschel formulation for the lower E_b/T_e case of shot 142371.

since that effect increases as the energetic ion energy decreases. The resulting FIDA density profiles are shown in Fig. 20(b). The \diamond -symbols mark the measured values, which are plotted alongside the expectations based on the classical and Pueschel models. Absolute comparisons between the modeled results are valid, and this shows that the energetic ion profile modification is as expected: enhancing diffusion at mid-radius leads to a reduction of the core energetic ion density. The measured FIDA density fits equally well to either modeled result. For the classical comparison, $\chi_{\text{red}}^2 = 4.4$ at the best-fit data scaling factor of 1.33, and for the Pueschel comparison, $\chi_{\text{red}}^2 = 6.1$ at a scale of 1.13. Motivated by the strong energy dependence in D_{EI} for this

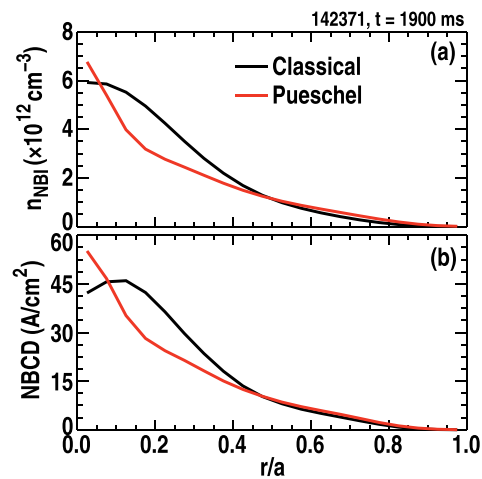


FIG. 19. Comparison between classically expected ($D_{EI} = 0$) and Pueschel model [D_{EI} from Eqs. (2) and (3)] profiles of (a) energetic ion density and (b) beam-driven current for the lower E_b/T_e case during on-axis injection.

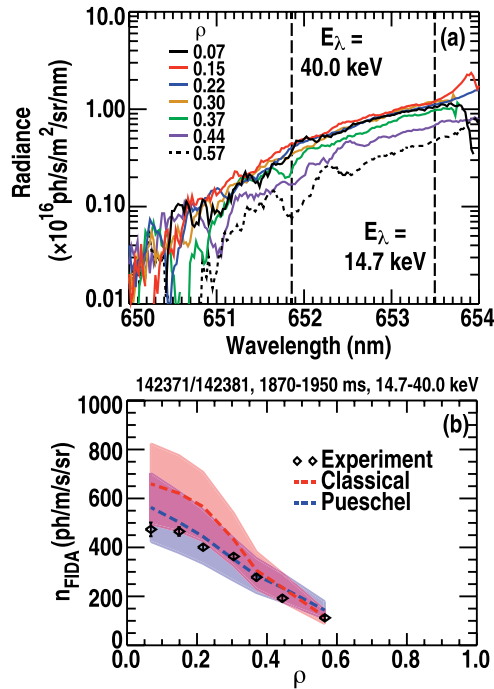


FIG. 20. (a) FIDA spectra from the lower E_b/T_e on-axis NBI case with vertical dashed bars representing the energetic ion tail region across $14.7 \leq E_i \leq 40.0$ keV. (b) FIDA density as measured (\diamond -symbols) and as modeled by the classical (dashed trace) or Pueschel formulation (solid trace).

case, we performed a separate set of fitting analyses based on the FIDA spectra. Since FIDA density is integrated spectra, it may be smoothing out significant differences between the measured and modeled spectra as a function of energy. The quality of the fit is calculated based on radiance only over the FIDA density integration range. These results are shown in Fig. 21. Figure 21(a) is a plot of the χ_{red}^2 for each radial chord. The measured spectra are a decent fit to each model, producing $\chi_{\text{red}}^2 < 5$. The classical spectra are systematically better fits than the Pueschel spectra, though this is a small improvement. In Fig. 21(b), a radial profile of the scaling factor corresponding to the best-fit spectrum is shown. There is little variation in the scaling factor across the radius. Two example spectra are shown in Fig. 21(c). Here, the modeled results are divided by the best-fit scaling factor in order to show the level of agreement between these spectra. Representative error bars on the measured spectra indicate the statistical uncertainty (the systematic uncertainty is addressed by the process of fitting). At $\rho = 0.22$, the best-fit classical profile is within the statistical uncertainty across the spectrum, while the Pueschel model produces too low a radiance at the lower energy limit. This suggests that the modeled turbulent transport of lower energy ions is greater than experimentally observed. For $\rho = 0.57$, both models produce excellent agreement with the shape of the measured FIDA spectrum.

An investigation of possible global effects due to turbulent transport is shown by Fig. 22. An autopower spectrum of density fluctuations measured by an interferometer is given in Fig. 22(a). The interferometer chord lies along the midplane and identifies apparent Alfvén cascades through

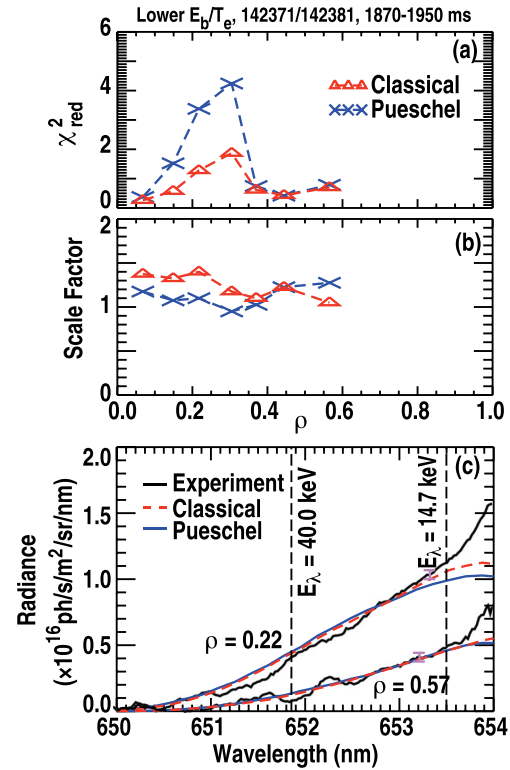


FIG. 21. Radial profiles of FIDA spectra fitting. (a) Quality of the scaled fit in terms of χ_{red}^2 . (b) Value of the scale factor (applied to the experimentally measured data) corresponding to the best fit. (c) Experimentally measured spectra compared to the best-fit model results for $\rho = 0.22$ and 0.57 .

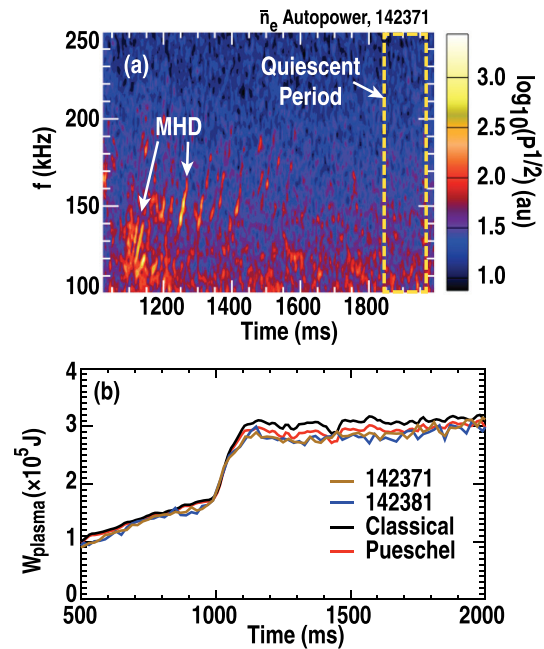


FIG. 22. (a) Autopower spectrum of line-averaged electron density fluctuations from shot 142371 indicating the presence of coherent modes through $t < 1600$ ms. The MHD-quiescent period is enclosed by the dashed rectangle. (b) Plasma stored energy from the paired shots (142371 and 142381) along with the TRANSP-calculated results from the Classical and Pueschel models.

$t \lesssim 1500$ ms. The MHD-quiescent period used for analysis of transport due to microturbulence, $1870 \leq t \leq 1950$ ms, is enclosed by the dashed rectangle. The total plasma stored energy is plotted in Fig. 22(b). The measured values for this pair of lower E_b/T_e shots (142371 and 142381) are shown to be equivalent. The results from TRANSP analysis based on the classical and Pueschel energetic ion transport anomalous diffusivities are also plotted. In this case, the classically expected stored energy is slightly larger than measured during the time range for which MHD is observed. This is to be expected since the thermal plasma energy is essentially an input to TRANSP (by way of the plasma profiles and equilibrium), while the energetic ion contribution is determined based on NUBEAM calculations. After $t = 1500$ ms, as the MHD activity decays away, the modeled stored energy traces approach the measured value. Even if the Pueschel model is perfectly describing energetic ion transport due to microturbulence, that transport has a smaller effect on stored energy than the spectrum of Alfvén eigenmodes driven in this low beam heating scenario of $P_{\text{NB}} = 2.5$ MW.

VI. DISCUSSION

A. Trends in the present results

A survey of all the shots studied is presented by the plot of χ_{red}^2 in Fig. 23. This plot concerns the fitting results of FIDA density and, in the case of the main ion D_x system, the FIDA brightness as a function of major radius. In the presence of weak Alfvén eigenmode activity (these AEs are driven by $P_{\text{NB}} = 2.5$ MW, while dedicated AE experiments⁴⁷ typically feature $P_{\text{NB}} \geq 5$ MW), the fit is poor and $\chi_{\text{red}}^2 > 20$. The FIDA profile at $E_b/T_e(0) \approx 10$, where we may theoretically expect to observe the most dramatic energetic ion transport by microturbulence, is fairly well described by a classical model using $D_{\text{EI}} = 0$. Furthermore, a turbulence model including a $D_{\text{EI}} \propto E_b/T_e$ treatment tends to produce a poorer fit. The on-axis beam injection case with $E_b/T_e(0) \approx 10$ is a suitable condition for testing models of turbulent energetic ion diffusion because the highest temperatures overlap with the location of the beam ions. Both the DEP and Pueschel models presented in this work determine D_{EI} based on the local temperature, though previous experimental results and Fig. 23 report E_b/T_e using the peak T_e . These are nearly the same in the on-axis case for which the lowest

value of E_b/T_e is achieved. The value of E_b in all cases is taken as the highest injection energy from a neutral beam during the time of interest (meaning much lower values of E_b/T_e are achieved during the slowing down process). The off-axis beam injection case at $E_b/T_e(0) \approx 30$ produces the worst fit to the classical model, though in this case, the inclusion of turbulent transport does not improve the agreement with experiment.

B. Consideration of previous results

Three experimental results are often cited as evidence for energetic ion transport by microturbulence. Given that the present work demonstrates that microturbulence-induced energetic ion transport is insignificant, it is useful to revisit the previous works. Results from AUG intended to show⁴³ that microturbulence enhances beam ion diffusion sufficiently well that off-axis NBCD is reduced. The plasma parameters are well characterized, and the experimental method successfully maintains comparable scenarios amongst changes in applied heating and plasma shape. Perhaps one challenge for this work is that there were no current drive or FIDA (or equivalent energetic ion profile diagnostic) measurements during the off-axis beam injection period. Current drive profiles were measured before and after the off-axis period, with TRANSP simulations used to infer the behavior during off-axis NBCD. Agreement between simulated and measured behavior in these before and after time periods was achieved by setting $D_{\text{EI}} = 0.5 \text{ m}^2/\text{s}$ constant in radius and energetic ion phase space. This value, especially when applied to ions of $E_b > 40$ keV, is much larger than the modeling performed with the DEP and Pueschel methods in the plasmas shown here. Electron temperature data from the AUG cases imply $T_e(0) > 3$ keV and show $T_e(\rho = 0.5) \approx 1.4$ keV, which are similar to the off-axis NBI shot of Sec. IV. While FIDA was not available during those experiments, a system has since been commissioned¹¹³ and observes classical energetic ion profiles during cases of $P_{\text{NB}} = 5$ MW in both on-axis and off-axis beam injection.¹¹⁴

Results from DIII-D claim to demonstrate a measurable energetic ion transport by microturbulence in both off-axis^{44,45,48} and on-axis⁴⁸ scenarios. The crucial aspect of these experiments is that the plasmas are MHD-quiescent. The largest NBCD differences between classical expectation and measurement are identified in the highest P_{NB} shots. In Ref. 45, it is noted that the highest P_{NB} shots feature either intermittent tearing modes or weak Alfvénic activity. Since any beam ion transport resulting from these fluctuations is not quantified, the result cannot be considered a strong argument for microturbulence-induced transport. Specifically, tearing modes are well known¹¹⁵ to reduce NBCD. Additional analysis of these high-power shots is presented in other publications,^{44,48} but still without quantifying the effects of coherent fluctuation activity. Another challenge for these experiments is that the off-axis NBCD is achieved by vertically shifting the plasmas. Since plasma profile diagnostics are fixed in real space, profile data are available only for $\rho > 0.4$. This leads to a great variability in the profiles as used for current drive and power balance calculations. An

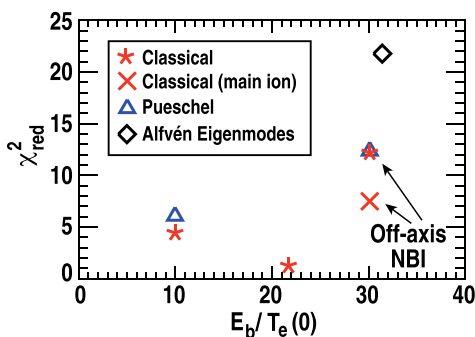


FIG. 23. Minimum value of χ_{red}^2 as a function of $E_b/T_e(0)$ for FIDA density profile fitting across the range of shots studied.

accounting of the variability in current drive across the possible range of central profiles should be provided. An on-axis beam injection example is presented in Ref. 48, where decreasing beam energy is reported to enhance the energetic ion transport by microturbulence because the injected beam ions feature smaller gyroradii. In this example, additional characterization of the beam injection and deposition may be necessary. For example, changing the neutral beam voltage can affect the injected power by producing a change in the fractional values of the 1/2 and 1/3 energy components. The development of advanced D_x systems allows for the measurement (or, technically, the inference) of neutral beam performance¹¹⁰ and greater confidence in the realized P_{NB} .

The third experiment concerns off-axis NBCD measurements⁴⁹ from JT-60U. Here, however, the anomalous behavior actually suggests a lack of microturbulence-induced transport. The measured beam driven current profiles are *overly* peaked compared to broader profiles produced in classical transport calculations. Furthermore, the measured current profiles peak for $\rho > 0.6$, and the shots featured $P_{NB} = 9$ MW. Taken together, these previous experimental results represent excellent work from three different facilities exercising wide arrays of diagnostic and modeling coverage. The ability of energetic ions to excite difficult-to-observe modes (e.g., multiple small amplitude Alfvén eigenmodes are known to enhance energetic ion transport¹¹⁶), along with the inability to measure energetic ion diffusion profiles directly, suggests that a particularly discerning review of such experimental results is warranted.

A final note in review of previous experiments concerns improvements to neutral beam current drive modeling. The choice of beam current shielding model^{117,118} in NUBEAM is known¹¹⁹ to vary the calculated beam driven current by up to 20%–30% for the plasma parameters of existing tokamaks. For consistency across shots, all of the NUBEAM calculations presented here are performed with the Honda shielding model.¹²⁰ The atomic physics options of NUBEAM have also been updated in recent years, and the present work uses the ADAS310 option.¹²¹ Future review of the DIII-D cases mentioned above will be conducted with these same options.

C. Consideration of “energetic” ions

While the shots presented here cover a wide range of parameter space, including that which should produce a measurable effect, it remains possible that other discharges will provide evidence for a turbulent transport effect. Theoretical scalings with E_b/T_e suggest that, eventually, an energetic ion slows down to a low enough energy that it experiences diffusion due to microturbulence. Indeed, it is known that in L-modes, the turbulent transport of the thermal plasma is orders of magnitude larger than neoclassical expectations, so we should expect that energetic ions experience turbulent diffusion before thermalizing. We, therefore, consider whether our diagnostic suite is capable of measuring such effects throughout the slowing down evolution of a beam ion population. Figure 24 is a contour of the difference between the energetic ion distributions calculated in the 4× Pueschel and classical cases. Negative values indicate a

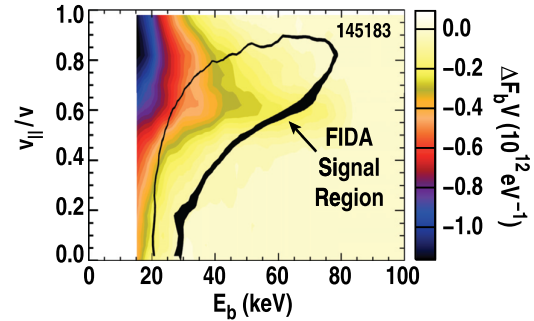


FIG. 24. Difference in the beam ion distribution, $F_b V$, between the 4× Pueschel case and the classical case in shot 145183. The contour labeled “FIDA Signal Region” represents the approximate boundary of the 0.08% contribution range of the FIDA phase space weighting shown in Fig. 3.

reduced number of beam ions within that phase space compared to the classical calculation. The solid outline labeled “FIDA Signal Region” is the $\sim 0.08\%$ contour level of the FIDA phase space weighting from Fig. 3. The largest change in the distribution (recalling this is the 4× increased model) occurs below $E_b = 20$ keV, where most of the change is found outside of the FIDA sensitivity range. It is reasonable to conclude that perhaps a transport enhancement due to microturbulence occurs, but that it manifests at energies only slightly above the thermal plasma and, therefore, produces no relevant or observable effects on the high-energy ion distribution. If so, then we should expect that measurements of this effect require the application of full D_x spectrum fitting, such as is possible with the main-ion charge exchange diagnostic¹¹⁰ that acquired the result shown in Fig. 10.

VII. CONCLUSIONS

The overwhelming indication from experiments, including those discussed in Sec. II A and the present work, is that microturbulence is an insignificant transport mechanism for energetic ions in tokamaks (limitations are detailed in the next paragraph). In much of the presently achievable tokamak parameter regime, in addition to the scenarios from DT-operation at TFTR and JET, energetic ion transport due to coherent modes is always dominant. For example, trapped energetic ions are theoretically expected to suffer less diffusion from microturbulence, yet they are easily transported out of confinement by ripple effects or neoclassical tearing modes.¹²² The experimental results presented in this work demonstrate that energetic ion diffusion due to microturbulence is a small effect in tokamak plasmas. Energetic ion profiles, as measured by FIDA systems, remain classical in truly MHD-quiet plasmas across a wide range of plasma parameters (e.g., E_b/T_e) and the character of microturbulence (e.g., ITG versus TEM). During off-axis neutral beam injection, the driven beam current is accurately modeled by NUBEAM for both strong turbulence in L-mode as presented here, and for high performance shots as shown in Ref. 7. These results are consistent with updated modeling that predicts⁷⁹ no significant energetic ion transport by microturbulence in ITER, while also identifying⁸² plasmas for further study in DEMO and TCV.

While this paper demonstrates that energetic ion transport by microturbulence is a negligible transport channel in tokamaks, there are caveats to that conclusion. First, the full parameter space of tokamak operation is not included here. The summary of results in Fig. 23 does not include the operating point of $E_b/T_e \lesssim 10$ at the location of off-axis beam injection. Such a scenario is not achieved in the other cited publications that have studied this problem, however, so this may not be an important issue. Second, it is possible that energetic ion profile diagnostics are not sensitive enough to accurately identify diffusion due to microturbulence. That could be true either because the diagnostics need to be improved, or because the transport effect itself is small. The $\Delta F_b V$ plot of Fig. 24 shows that the largest turbulence-induced perturbation of the energetic ion distribution occurs at energies commonly below the FIDA resolvable limit. This is also demonstrated by the modeled FIDA density profile variation of Fig. 16(b), in which a very large (modeled) turbulent diffusion produces a reduction in the core ($\approx 25\%$) that is within the uncertainty of the synthetic diagnostic. From this, it is suggested that further development of synthetic FIDA diagnostics is absolutely necessary to gain confidence in any future identification of turbulent transport. The third caveat is that the principle of energetic ion interaction with small-scale turbulent fluctuations is well established, so the present lack of observable effect must be placed within that physical context. Basic plasma devices clearly demonstrate this transport effect, though since the fluctuation levels routinely reach 100%, perhaps that is the most relevant difference compared to tokamaks where this level is closer to 1%. Recent work on DIII-D finds that an energetic ion population (treated as a hot Maxwellian) must be included in gyrokinetic simulations of high performance QH-modes in order to more closely reproduce the experimentally measured energy fluxes.¹²³ It was noted that this inclusion is only necessary in those shots for which the energetic ion density reached large values of $n_{EI} \approx 0.25n_e$, however, and the interpretation is that this is a dilution effect (i.e., not indicative of an interaction between energetic ions and microturbulence).

The advances in physics understanding concerning the interaction between small-scale turbulence and energetic ions may find application in other areas. Energetic electrons have smaller gyroradii compared to energetic ions, and might therefore be expected to diffuse significantly in the presence of microturbulence. Electron cyclotron heating and current drive is capable of producing a narrower spatial distribution than a neutral beam, which might make it easier to measure broadening due to diffusion.¹²⁴ A recent study¹²⁵ examines this process for runaway electrons in the presence of magnetic fluctuations and identifies enhanced transport.

In summary, investigations of energetic ion transport by microturbulence have led to the development of models that predict the resulting diffusivity as a function of ion energy and pitch. This represents a greater modeling ability than is presently available for transport due to Alfvén eigenmodes or other MHD. Certainly, the possible identification of plasma modification due to turbulent energetic ion transport in other scenarios will require the application of these formulations. While the DEP and Pueschel models are readily

accessible to experiments, it is also possible to conduct gyrokinetic simulations that simultaneously address the development of the turbulent field and the resulting energetic ion transport. These tools represent a major advance in the area of energetic particle transport in tokamaks. In terms of ITER, the results of this paper suggest that energetic ion concerns should give priority to MHD and other non-microturbulence effects.

ACKNOWLEDGMENTS

This work was supported in part by the US Department of Energy under DE-FC02-04ER54698, DE-FC02-99ER54512, DE-FG03-97ER54415, DE-FG02-07ER54917, DE-AC02-09CH11466, SC-G903402, DE-FG02-08ER54984, DE-AC52-07NA27344, DE-FG02-89ER53296, DE-FG02-08ER54999, and DE-AC05-00OR22725. The authors are grateful to M. Albergante, A. Fasoli, S. Jardin, and ITPA Energetic Particles Group for thoughtful discussions on this topic, R. J. Groebner for assisting with the processing of CER data, and B. Geiger and M. García-Muñoz for sharing their results from ASDEX Upgrade. The experimental work was made possible by the extraordinary personnel of the DIII-D National Fusion Facility.

¹J. Wesson, *Tokamaks*, 4th ed., International Series of Monographs on Physics (Oxford Science Publications, 2011).

²M. Shimada, D. J. Campbell, V. Mukhovatov, M. Fujiwara, N. Kirneva, K. Lackner, M. Nagami, V. D. Pustovitov, N. Uckan, J. Wesley, N. Asakura, A. E. Costley, A. J. H. Donné, E. J. Doyle, A. Fasoli, C. Gormezano, Y. Gribov, O. Gruber, T. C. Hender, W. Houlberg, S. Ide, Y. Kamada, A. Leonard, B. Lipschultz, A. Loarte, K. Miyamoto, V. Mukhovatov, T. H. Osborne, A. Polevoi, and A. C. C. Sips, *Nucl. Fusion* **47**, S1 (2007).

³W. W. Heidbrink, *Phys. Plasmas* **15**, 055501 (2008).

⁴W. W. Heidbrink and G. J. Sadler, *Nucl. Fusion* **34**, 535 (1994).

⁵B. N. Breizman and S. E. Sharapov, *Plasma Phys. Controlled Fusion* **53**, 054001 (2011).

⁶T. Suzuki, R. J. Akers, D. A. Gates, S. Günter, W. W. Heidbrink, J. Hobirk, T. C. Luce, M. Murakami, J. M. Park, M. Turnyanskiy, and ITPA Integrated Operation Scenarios group members and experts, *Nucl. Fusion* **51**, 083020 (2011).

⁷J. M. Park, M. Murakami, C. C. Petty, W. W. Heidbrink, M. A. Van Zeeland, D. C. Pace, R. Prater, J. R. Ferron, T. H. Osborne, C. T. Holcomb, G. L. Jackson, T. W. Petrie, B. A. Grierson, C. J. Murphy, and T. Suzuki, in *Proc. 24th IAEA Conf. on Fusion Energy* (San Diego, United States, 2012), paper EX/P2-13.

⁸J. L. Luxon, *Nucl. Fusion* **42**, 614 (2002).

⁹C. M. Greenfield and DIII-D Team, *Nucl. Fusion* **51**, 094009 (2011).

¹⁰A. Fasoli, C. Gormenzano, H. L. Berk, B. Breizman, S. Briguglio, D. S. Darrow, N. Gorelenkov, W. W. Heidbrink, A. Jaun, S. V. Kononov, R. Nazikian, J.-M. Noterdaeme, S. Sharapov, K. Shinohara, D. Testa, K. Tobita, Y. Todo, G. Vlad, and F. Zonca, *Nucl. Fusion* **47**, S264 (2007).

¹¹W. Gekelman, H. Pfister, Z. Lucky, J. Bamber, D. Leneman, and J. Maggs, *Rev. Sci. Instrum.* **62**, 2875 (1991).

¹²L. Zhao, W. W. Heidbrink, H. Boehmer, R. Mc Williams, D. Leneman, and S. Vincena, *Phys. Plasmas* **12**, 052108 (2005).

¹³A. T. Burke, J. E. Maggs, and G. J. Morales, *Phys. Rev. Lett.* **81**, 3659 (1998).

¹⁴S. Zhou, W. W. Heidbrink, H. Boehmer, R. Mc Williams, T. Carter, S. Vincena, S. K. P. Tripathi, P. Popovich, B. Friedman, and F. Jenko, *Phys. Plasmas* **17**, 092103 (2010).

¹⁵S. Zhou, W. W. Heidbrink, H. Boehmer, R. Mc Williams, T. A. Carter, S. Vincena, and S. K. P. Tripathi, *Phys. Plasmas* **18**, 082104 (2011).

¹⁶A. Fasoli, B. Labit, M. McGrath, S. H. Müller, G. Plyushchev, M. Pedestà, and F. M. Poli, *Phys. Plasmas* **13**, 055902 (2006).

- ¹⁷A. Fasoli, A. Burckel, L. Federspiel, I. Furno, K. Gustafson, D. Iraj, B. Labit, J. Loizu, G. Plyushchev, P. Ricci, C. Theiler, A. Diallo, S. H. Müller, M. Podestà, and F. Poli, *Plasma Phys. Controlled Fusion* **52**, 124020 (2010).
- ¹⁸D. A. D'Ippolito, J. R. Myra, and S. J. Zweben, *Phys. Plasmas* **18**, 060501 (2011).
- ¹⁹K. Gustafson, P. Ricci, I. Furno, and A. Fasoli, *Phys. Rev. Lett.* **108**, 035006 (2012).
- ²⁰K. Gustafson and P. Ricci, *Phys. Plasmas* **19**, 032304 (2012).
- ²¹K. Gustafson, P. Ricci, A. Bovet, I. Furno, and A. Fasoli, *Phys. Plasmas* **19**, 062306 (2012).
- ²²R. J. Hawryluk, S. Batha, W. Blanchard, M. Beer, M. G. Bell, R. E. Bell, H. Berk, S. Bernabei, M. Bitter, B. Breizman, N. L. Bretz, R. Budny, C. E. Bush, J. Callen, R. Camp, S. Cauffman, Z. Chang, C. Z. Cheng, D. S. Darrow, R. O. Dendy, W. Dorland, H. Duong, P. C. Efthimion, D. Ernst, N. J. Fisch, R. Fisher, R. J. Fonck, E. D. Fredrickson, G. Y. Fu, H. P. Furth, N. N. Gorelenkov, B. Grek, L. R. Grisham, G. W. Hammett, G. R. Hanson, H. W. Herrmann, M. C. Herrmann, K. W. Hill, J. Hogan, J. C. Hosea, W. A. Houlberg, M. Hughes, R. A. Hulse, D. L. Jassby, F. C. Jobs, D. W. Johnson, R. Kaita, S. Kaye, J. S. Kim, M. Kissick, A. V. Krasilnikov, H. Kugel, A. Kumar, B. Leblanc, F. M. Levinton, C. Ludescher, R. P. Majeski, J. Manickam, D. K. Mansfield, E. Mazzucato, J. McCesney, D. C. McCune, K. M. McGuire, D. M. Meade, S. S. Medley, R. Mika, D. R. Mikkelsen, S. V. Mirnov, D. Mueller, A. Nagy, G. A. Navratil, R. Nazikian, M. Okabayashi, H. K. Park, W. Park, S. F. Paul, G. Pearson, M. P. Petrov, C. K. Phillips, M. Phillips, A. T. Ramsey, M. H. Redi, G. Rewoldt, S. Reznik, A. L. Roquemore, J. Rogers, E. Ruskov, S. A. Sabbagh, M. Sasao, G. Schilling, J. Schivell, G. L. Schmidt, S. D. Scott, I. Semenov, C. H. Skinner, T. Stevenson, B. C. Stratton, J. D. Strachan, W. Stodiek, E. Synakowski, H. Takahashi, W. Tang, G. Taylor, M. E. Thompson, S. V. Goeler, A. V. Halle, R. T. Walters, R. White, R. M. Wieland, M. Williams, J. R. Wilson, K. L. Wong, G. A. Wurden, M. Yamada, V. Yavorski, K. M. Young, L. Zakharov, M. C. Zarnstorff, and S. J. Zweben, *Phys. Plasmas* **5**, 1577 (1998).
- ²³S. J. Zweben, R. L. Boivin, C.-S. Chang, G. W. Hammett, and H. E. Mynick, *Nucl. Fusion* **31**, 2219 (1991).
- ²⁴S. J. Zweben, D. S. Darrow, E. D. Fredrickson, and H. E. Mynick, *Nucl. Fusion* **33**, 705 (1993).
- ²⁵S. J. Zweben, C. E. Bush, C. S. Chang, Z. Chang, D. S. Darrow, E. D. Fredrickson, H. W. Herrmann, H. E. Mynick, J. Schivell, M. Bell, R. Boivin, R. V. Budny, C. Z. Cheng, D. Ernst, G. Hammett, L. C. Johnson, D. McCune, M. Murakami, D. K. Owens, J. Park, C.-K. Phillips, M. H. Redi, S. Scott, J. D. Strachan, G. Taylor, M. Tuszewski, R. B. White, J. R. Wilson, and M. Zarnstorff, *Phys. Plasmas* **1**, 1469 (1994).
- ²⁶V. A. Yavorski, J. W. W. Edenstrasser, V. Ya. Goloborod'ko, S. N. Reznik, and S. J. Zweben, *Nucl. Fusion* **38**, 1565 (1998).
- ²⁷G. McKee, R. Fonck, B. Stratton, R. Bell, R. Budny, C. Bush, B. Grek, D. Johnson, H. Park, A. Ramsey, E. Synakowski, and G. Taylor, *Phys. Rev. Lett.* **75**, 649 (1995).
- ²⁸G. R. McKee, R. J. Fonck, B. C. Stratton, R. V. Budny, Z. Chang, and A. T. Ramsey, *Nucl. Fusion* **37**, 501 (1997).
- ²⁹S. J. Zweben, D. S. Darrow, H. W. Herrmann, S. H. Batha, R. V. Budny, C.-S. Chang, Z. Chang, E. D. Fredrickson, D. L. Jassby, L. C. Johnson, F. M. Levinton, H. E. Mynick, D. K. Owens, J. F. Schivell, S. D. Scott, M. H. Redi, J. D. Strachan, K. Tobita, and K. M. Young, *Nucl. Fusion* **35**, 893 (1995).
- ³⁰See <http://w3.pppl.gov/transp>, the official homepage of TRANSP, for information concerning the models and methods employed, in addition to usage documentation.
- ³¹E. Ruskov, W. W. Heidbrink, and R. V. Budny, *Nucl. Fusion* **35**, 1099 (1995).
- ³²W. W. Heidbrink, C. W. Barnes, G. W. Hammett, Y. Kusama, S. D. Scott, M. C. Zarnstorff, L. C. Johnson, D. McCune, S. S. Medley, H. K. Park, A. L. Roquemore, J. D. Strachan, and G. Taylor, *Phys. Fluids B* **3**, 3167 (1991).
- ³³E. Ruskov, W. W. Heidbrink, D. McCune, and L. Johnson, *Plasma Phys. Controlled Fusion* **38**, 389 (1996).
- ³⁴E. Ruskov, W. W. Heidbrink, R. V. Budny, and D. C. McCune, *Nucl. Fusion* **35**, 1517 (1995).
- ³⁵E. Ruskov, M. Bell, R. V. Budny, D. C. McCune, S. S. Medley, M. H. Redi, S. Scott, E. J. Synakowski, S. von Goeler, R. B. White, and S. J. Zweben, *Phys. Rev. Lett.* **82**, 924 (1999).
- ³⁶H. L. Berk, D. N. Borba, B. N. Breizman, S. D. Pinches, and S. E. Sharapov, *Phys. Rev. Lett.* **87**, 185002 (2001).
- ³⁷S. E. Sharapov, B. Alper, H. L. Berk, D. N. Borba, B. N. Breizman, C. D. Challis, A. Fasoli, N. C. Hawkes, T. C. Hender, J. Mailoux, S. D. Pinches, D. Testa, and Contributors to the EFDA-JET Work Programme, *Phys. Plasmas* **9**, 2027 (2002).
- ³⁸S. E. Sharapov, B. Alper, J. Fessey, N. C. Hawkes, N. P. Young, R. Nazikian, G. J. Kramer, D. N. Borba, S. Hacquin, E. De La Luna, S. D. Pinches, J. Rapp, D. Testa, and JET-EFDA Contributors, *Phys. Rev. Lett.* **93**, 165001 (2004).
- ³⁹M. A. Van Zeeland, W. W. Heidbrink, R. Nazikian, W. M. Solomon, M. E. Austin, H. L. Berk, N. N. Gorelenkov, C. T. Holcomb, A. W. Hyatt, G. J. Kramer, J. Lohr, M. A. Makowski, G. R. McKee, C. C. Petty, S. E. Sharapov, and T. L. Rhodes, *Plasma Phys. Controlled Fusion* **50**, 035009 (2008).
- ⁴⁰K. Tobita, H. Harano, T. Nishitani, T. Fujita, K. Tani, T. Oikawa, H. Shirai, and Y. Kusama, *Nucl. Fusion* **37**, 1583 (1997).
- ⁴¹H. H. Duong and W. W. Heidbrink, *Nucl. Fusion* **33**, 211 (1993).
- ⁴²Y. F. Baranov, I. Jenkins, B. Alper, C. D. Challis, S. Conroy, V. Kiptily, J. Ongena, S. Popovichev, P. Smeulders, E. Surrey, K.-D. Zastrow, and JET-EFDA Contributors, *Plasma Phys. Controlled Fusion* **51**, 044004 (2009).
- ⁴³S. Günter, G. Conway, S. daGraça, H.-U. Fahrback, C. Forest, M. García-Muñoz, T. Hauff, J. Hobirk, V. Igochine, F. Jenko, K. Lackner, P. Lauber, P. McCarthy, M. Maraschek, P. Martin, E. Poli, K. Sassenberg, E. Strumberger, G. Tardini, E. Wolfrum, H. Zohm, and ASDEX-Upgrade Team, *Nucl. Fusion* **47**, 920 (2007).
- ⁴⁴W. W. Heidbrink, J. M. Park, M. Murakami, C. C. Petty, C. Holcomb, and M. A. Van Zeeland, *Phys. Rev. Lett.* **103**, 175001 (2009).
- ⁴⁵W. W. Heidbrink, M. Murakami, J. M. Park, C. C. Petty, M. A. Van Zeeland, J. H. Yu, and G. R. McKee, *Plasma Phys. Controlled Fusion* **51**, 125001 (2009).
- ⁴⁶M. Murakami, M. R. Wade, J. C. DeBoo, C. M. Greenfield, T. C. Luce, M. A. Makowski, C. C. Petty, G. M. Staebler, T. S. Taylor, M. E. Austin, D. R. Baker, R. V. Budny, K. H. Burrell, T. A. Casper, M. Choi, J. R. Ferron, A. M. Garofalo, I. A. Gorelov, R. J. Groebner, R. J. La Haye, A. W. Hyatt, R. J. Jayakumar, K. Kajiwara, J. E. Kinsey, L. L. Lao, J. Lohr, D. McCune, R. I. Pinsker, P. A. Politzer, R. Prater, H. E. St. John, and W. P. West, *Phys. Plasmas* **10**, 1691 (2003).
- ⁴⁷M. A. Van Zeeland, W. W. Heidbrink, R. K. Fisher, M. García-Muñoz, G. J. Kramer, D. C. Pace, R. B. White, S. Aekasompolo, M. E. Austin, J. E. Boom, I. G. J. Classen, S. daGraça, B. Geiger, M. Gorelenkova, N. N. Gorelenkov, A. W. Hyatt, N. Luhmann, M. Maraschek, G. R. McKee, R. A. Moyer, C. M. Muscatello, R. Nazikian, H. Park, S. Sharapov, W. Suttrop, G. Tardini, B. J. Tobias, Y. B. Zhu, and DIII-D and ASDEX Upgrade Teams, *Phys. Plasmas* **18**, 056114 (2011).
- ⁴⁸D. C. Pace, R. K. Fisher, M. García-Muñoz, W. W. Heidbrink, G. R. McKee, M. Murakami, C. M. Muscatello, R. Nazikian, J. M. Park, C. C. Petty, T. L. Rhodes, G. M. Staebler, M. A. Van Zeeland, R. E. Waltz, R. B. White, J. H. Yu, W. Zhang, and Y. B. Zhu, *Nucl. Fusion* **51**, 043012 (2011).
- ⁴⁹T. Suzuki, S. Ide, T. Oikawa, T. Fujita, M. Ishikawa, M. Seki, G. Matsunaga, T. Hatae, O. Naito, K. Hamamatsu, M. Sueoka, H. Hosoyama, M. Nakazato, and JT-60 Team, *Nucl. Fusion* **48**, 045002 (2008).
- ⁵⁰R. Basu, T. Jessen, V. Naulin, and J. J. Rasmussen, *Phys. Plasmas* **10**, 2696 (2003).
- ⁵¹R. B. White and H. E. Mynick, *Phys. Fluids B* **1**, 980 (1989).
- ⁵²T. Hauff, M. J. Pueschel, T. Dannert, and F. Jenko, *Phys. Rev. Lett.* **102**, 075004 (2009).
- ⁵³D. J. Sigmar, F. Gang, R. Gormley, and C. T. Hsu, *Plasma Phys. Controlled Fusion* **34**, 1845 (1992).
- ⁵⁴D. Sigmar, R. Gormley, and G. Kamelander, *Nucl. Fusion* **33**, 677 (1993).
- ⁵⁵H. Naitou, T. Kamimura, and J. M. Dawson, *J. Phys. Soc. Jpn.* **46**, 258 (1979).
- ⁵⁶G. Manfredi and R. O. Dendy, *Phys. Rev. Lett.* **76**, 4360 (1996).
- ⁵⁷G. Manfredi and R. O. Dendy, *Phys. Plasmas* **4**, 628 (1997).
- ⁵⁸S. V. Annibaldi, G. Manfredi, and R. O. Dendy, *Phys. Plasmas* **9**, 791 (2002).
- ⁵⁹M. Vlad, F. Spineanu, S.-I. Itoh, M. Yagi, and K. Itoh, *Plasma Phys. Controlled Fusion* **47**, 1015 (2005).
- ⁶⁰T. Hauff and F. Jenko, *Phys. Plasmas* **13**, 102309 (2006).
- ⁶¹T. Dannert, S. Günter, T. Hauff, F. Jenko, X. Lapillonne, and P. Lauber, *Phys. Plasmas* **15**, 062508 (2008).
- ⁶²J. Candy and R. E. Waltz, *J. Comput. Phys.* **186**, 545 (2003).

- ⁶³C. Estrada-Mila, J. Candy, and R. E. Waltz, *Phys. Plasmas* **13**, 112303 (2006).
- ⁶⁴T. Dannert and F. Jenko, *Phys. Plasmas* **12**, 072309 (2005).
- ⁶⁵T. Hauff and F. Jenko, *Phys. Plasmas* **14**, 092301 (2007).
- ⁶⁶T. Hauff and F. Jenko, *Phys. Plasmas* **15**, 112307 (2008).
- ⁶⁷Z. Lin, T. S. Hahn, W. W. Lee, W. M. Tang, and R. B. White, *Science* **281**, 1835 (1998).
- ⁶⁸W. Zhang, Z. Lin, and L. Chen, *Phys. Rev. Lett.* **101**, 095001 (2008).
- ⁶⁹W. Zhang, V. Decyk, I. Holod, Y. Xiao, Z. Lin, and L. Chen, *Phys. Plasmas* **17**, 055902 (2010).
- ⁷⁰W. Zhang, Z. Lin, and L. Chen, *Phys. Rev. Lett.* **107**, 239501 (2011).
- ⁷¹F. Jenko, T. Hauff, M. J. Pueschel, and T. Dannert, *Phys. Rev. Lett.* **107**, 239502 (2011).
- ⁷²J. Chowdhury, W. Wang, S. Ethier, J. Manickam, and R. Ganesh, *Phys. Plasmas* **18**, 112510 (2011).
- ⁷³J. Chowdhury, W. Wang, S. Ethier, J. Manickam, and R. Ganesh, *Phys. Plasmas* **19**, 042503 (2012).
- ⁷⁴R. E. Waltz, E. M. Bass, and G. M. Staebler, *Phys. Plasmas* **20**, 042510 (2013).
- ⁷⁵J. M. Dewhurst, B. Hnat, and R. O. Dendy, *Plasma Phys. Controlled Fusion* **52**, 025004 (2010).
- ⁷⁶C. Angioni and A. G. Peeters, *Phys. Plasmas* **15**, 052307 (2008).
- ⁷⁷M. Albergante, J. P. Graves, A. Fasoli, F. Jenko, and T. Dannert, *Phys. Plasmas* **16**, 112301 (2009).
- ⁷⁸M. Albergante, J. Graves, A. Fasoli, and X. Lapillonne, *Nucl. Fusion* **50**, 084013 (2010).
- ⁷⁹M. Albergante, J. P. Graves, A. Fasoli, M. Jucker, X. Lapillonne, and W. A. Cooper, *Plasma Phys. Controlled Fusion* **53**, 054002 (2011).
- ⁸⁰D. M. Thomas, *Phys. Plasmas* **19**, 056118 (2012).
- ⁸¹T. Inoue, M. Taniguchi, T. Morishita, M. Dairaku, M. Hanada, T. Imai, M. Kashiwagi, K. Sakamoto, T. Seki, and K. Watanabe, *Nucl. Fusion* **45**, 790 (2005).
- ⁸²M. Albergante, A. Fasoli, J. Graves, S. Brunner, and W. Cooper, *Nucl. Fusion* **52**, 094016 (2012).
- ⁸³D. J. Ward, *Plasma Phys. Controlled Fusion* **52**, 124033 (2010).
- ⁸⁴A. Fasoli, *Nucl. Fusion* **49**, 104005 (2009).
- ⁸⁵A. N. Karpushov, B. P. Duval, R. Chavan, E. Fable, J.-M. Mayor, O. Sauter, and H. Weisen, *Fusion Eng. Design* **86**, 868 (2011).
- ⁸⁶M. Albergante, "Interaction between fast ions and microturbulence in thermonuclear devices: Theory and modelling," Ph.D. dissertation (École Polytechnique Fédérale de Lausanne, 2011).
- ⁸⁷M. J. Pueschel, F. Jenko, M. Schneller, T. Hauff, S. Günter, and G. Tardini, *Nucl. Fusion* **52**, 103018 (2012).
- ⁸⁸R. Nazikian, N. N. Gorelenkov, B. Alper, H. L. Berk, D. Borba, R. V. Budny, G. Y. Fu, W. W. Heidbrink, G. J. Kramer, M. A. Makowski, S. D. Pinches, S. E. Sharapov, W. M. Solomon, E. J. Strait, R. B. White, M. A. Van Zeeland, and JET-EFDA Contributors, *Phys. Plasmas* **15**, 056107 (2008).
- ⁸⁹M. A. Van Zeeland, R. L. Boivin, T. N. Carlstrom, T. Deterly, and D. K. Finkenthal, *Rev. Sci. Instrum.* **77**, 10F325 (2006).
- ⁹⁰M. E. Austin and J. Lohr, *Rev. Sci. Instrum.* **74**, 1457 (2003).
- ⁹¹W. W. Heidbrink, P. L. Taylor, and J. A. Phillips, *Rev. Sci. Instrum.* **68**, 536 (1997).
- ⁹²W. W. Heidbrink, M. A. Van Zeeland, B. A. Grierson, C. M. Muscatello, J. M. Park, C. C. Petty, R. Prater, and Y. B. Zhu, *Nucl. Fusion* **52**, 094005 (2012).
- ⁹³Y. Luo, W. W. Heidbrink, K. H. Burrell, D. H. Kaplan, and P. Gohil, *Rev. Sci. Instrum.* **78**, 033505 (2007).
- ⁹⁴W. W. Heidbrink, *Rev. Sci. Instrum.* **81**, 10D727 (2010).
- ⁹⁵W. W. Heidbrink, Y. Luo, K. H. Burrell, R. W. Harvey, R. I. Pinsky, and E. Ruskov, *Plasma Phys. Controlled Fusion* **49**, 1457 (2007).
- ⁹⁶M. Salewski, S. K. Nielsen, H. Bindslev, V. Furtula, N. N. Gorelenkov, S. B. Korsholm, F. Leipold, F. Meo, P. K. Michelsen, D. Moseev, and M. Stejner, *Nucl. Fusion* **51**, 083014 (2011).
- ⁹⁷Y. Luo, W. W. Heidbrink, K. H. Burrell, E. Ruskov, and W. M. Solomon, *Phys. Plasmas* **14**, 112503 (2007).
- ⁹⁸G. McKee, R. Ashley, R. Durst, R. Fonck, M. Jakubowski, K. Tritz, K. Burrell, C. Greenfield, and J. Robinson, *Rev. Sci. Instrum.* **70**, 913 (1999).
- ⁹⁹J. C. Hillesheim, W. A. Peebles, T. L. Rhodes, L. Schmitz, T. A. Carter, P.-A. Gourdain, and G. Wang, *Rev. Sci. Instrum.* **80**, 083507 (2009).
- ¹⁰⁰A. E. White, L. Schmitz, W. A. Peebles, T. A. Carter, T. L. Rhodes, E. J. Doyle, P. A. Gourdain, J. C. Hillesheim, G. Wang, C. Holland, G. R. Tynan, M. E. Austin, G. R. McKee, M. W. Shafer, K. H. Burrell, J. Candy, J. C. DeBoo, R. Prater, G. M. Staebler, R. E. Waltz, and M. A. Makowski, *Rev. Sci. Instrum.* **79**, 103505 (2008).
- ¹⁰¹J. C. Hillesheim, W. A. Peebles, T. L. Rhodes, L. Schmitz, A. E. White, and T. A. Carter, *Rev. Sci. Instrum.* **81**, 10D907 (2010).
- ¹⁰²A. E. White, W. A. Peebles, T. L. Rhodes, C. H. Holland, G. Wang, L. Schmitz, T. A. Carter, J. C. Hillesheim, E. J. Doyle, L. Zeng, G. R. McKee, G. M. Staebler, R. E. Waltz, J. C. DeBoo, C. C. Petty, and K. H. Burrell, *Phys. Plasmas* **17**, 056103 (2010).
- ¹⁰³R. Goldston, D. McCune, H. Towner, S. Davis, R. Hawryluk, and G. Schmidt, *J. Comput. Phys.* **43**, 61 (1981).
- ¹⁰⁴A. Pankin, D. McCune, R. Andre, G. Bateman, and A. Kritiz, *Comput. Phys. Commun.* **159**, 157 (2004).
- ¹⁰⁵W. W. Heidbrink, D. Liu, Y. Luo, E. Ruskov, and B. Geiger, *Comput. Phys. Commun.* **10**, 716 (2011).
- ¹⁰⁶M. A. Van Zeeland, N. N. Gorelenkov, W. W. Heidbrink, G. J. Kramer, D. A. Spong, M. E. Austin, R. K. Fisher, M. García Muñoz, M. Gorelenkova, N. Luhmann, M. Murakami, R. Nazikian, D. C. Pace, J. M. Park, B. J. Tobias, and R. B. White, *Nucl. Fusion* **52**, 094023 (2012).
- ¹⁰⁷D. M. Ponce-Marquez, B. D. Bray, T. M. Deterly, C. Liu, and D. Eldon, *Rev. Sci. Instrum.* **81**, 10D525 (2010).
- ¹⁰⁸W. M. Solomon, K. H. Burrell, R. Feder, A. Nagy, P. Gohil, and R. J. Groebner, *Rev. Sci. Instrum.* **79**, 10F531 (2008).
- ¹⁰⁹J. E. Kinsey, G. M. Staebler, and R. E. Waltz, *Phys. Plasmas* **15**, 055908 (2008).
- ¹¹⁰B. A. Grierson, K. H. Burrell, C. Chrystal, R. J. Groebner, D. H. Kaplan, W. W. Heidbrink, J. M. Muñoz Burgos, N. A. Pablant, W. M. Solomon, and M. A. Van Zeeland, *Rev. Sci. Instrum.* **83**, 10D529 (2012).
- ¹¹¹The FIDASIM Users Group currently includes researchers from the DIII-D, AUG, MAST, and NSTX facilities.
- ¹¹²T. L. Rhodes, C. Holland, S. P. Smith, A. E. White, K. H. Burrell, J. Candy, J. C. DeBoo, E. J. Doyle, J. C. Hillesheim, J. E. Kinsey, G. R. McKee, D. Mikkelsen, W. A. Peebles, C. C. Petty, R. Prater, S. Parker, Y. Chen, L. Schmitz, G. M. Staebler, R. E. Waltz, G. Wang, Z. Yan, and L. Zeng, *Nucl. Fusion* **51**, 063022 (2011).
- ¹¹³B. Geiger, M. García-Muñoz, W. W. Heidbrink, R. M. McDermott, G. Tardini, R. Dux, R. Fischer, V. Igochine, and ASDEX Upgrade Team, *Plasma Phys. Controlled Fusion* **53**, 065010 (2011).
- ¹¹⁴B. Geiger, M. García-Muñoz, R. Dux, R. M. McDermott, G. Tardini, J. Hobirk, T. Lunt, W. W. Heidbrink, F. Ryter, and ASDEX Upgrade Team, in *39th EPS Conf. and 16th Int. Congress on Plasma Physics* (2012), paper P4.068.
- ¹¹⁵C. B. Forest, J. R. Ferron, T. Gianakon, R. W. Harvey, W. W. Heidbrink, A. W. Hyatt, R. J. La Haye, M. Murakami, P. A. Politzer, and H. E. St. John, *Phys. Rev. Lett.* **79**, 427 (1997).
- ¹¹⁶R. B. White, N. Gorelenkov, W. W. Heidbrink, and M. A. Van Zeeland, *Phys. Plasmas* **17**, 056107 (2010).
- ¹¹⁷S. P. Hirshman, *Phys. Fluids* **21**, 1295 (1978).
- ¹¹⁸Y. R. Lin-Liu and F. L. Hinton, *Phys. Plasmas* **4**, 4179 (1997).
- ¹¹⁹D. C. McCune, TRANSP User Group, January 27, 2011.
- ¹²⁰M. Honda, M. Kikuchi, and M. Azumi, *Nucl. Fusion* **52**, 023021 (2012).
- ¹²¹See <http://w3.pppl.gov/pshare/help/bodytransphlp.html#outlet277.html> for TRANSP Help: Deposition Atomic Physics Options.
- ¹²²E. Poli, M. García-Muñoz, H.-U. Fahrbach, S. Günter, and ASDEX Upgrade Team, *Phys. Plasmas* **15**, 032501 (2008).
- ¹²³C. Holland, C. C. Petty, L. Schmitz, K. H. Burrell, G. R. McKee, T. L. Rhodes, and J. Candy, *Nucl. Fusion* **52**, 114007 (2012).
- ¹²⁴C. C. Petty, M. E. Austin, J. Lohr, T. C. Luce, M. A. Makowski, R. Prater, R. W. Harvey, and A. P. Smirnov, *Fusion Sci. Technol.* **57**, 10 (2010).
- ¹²⁵S. S. Abdullaev, K. H. Finken, and M. Forster, *Phys. Plasmas* **19**, 072502 (2012).